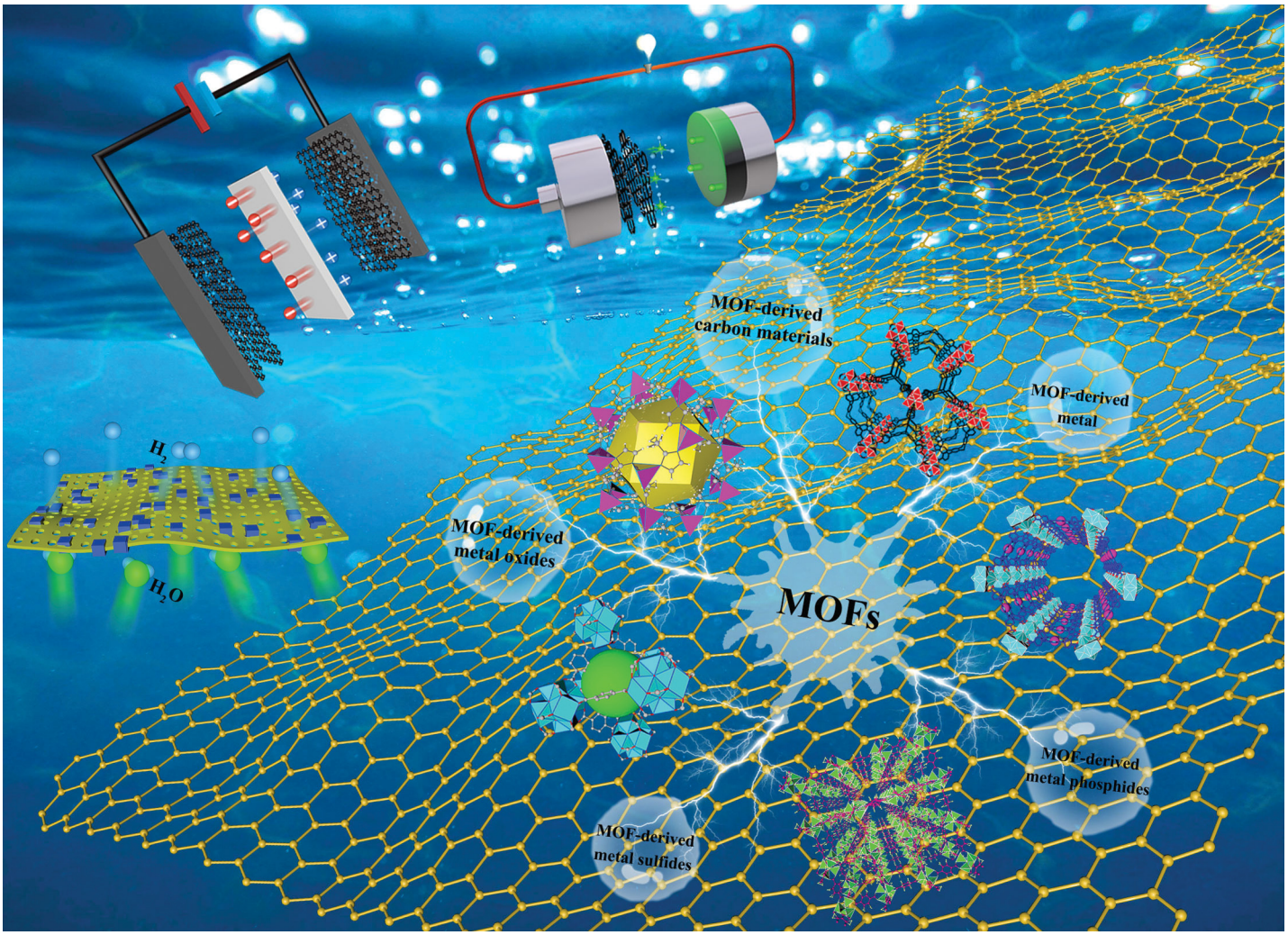

Showcasing research from Professor Yuxi Xu's laboratory, School of Engineering, Westlake University, Hangzhou, China

Three-dimensional graphene/metal–organic framework composites for electrochemical energy storage and conversion

This feature article summarizes the recent research progress in the preparation methods of 3DG/MOF composites and their derivatives. Their applications in the fields of electrochemical energy storage and conversion, such as batteries, supercapacitors, and electrocatalysis, are also discussed.

As featured in:

See Yumei Ren and Yuxi Xu, *Chem. Commun.*, 2023, **59**, 6475.

ROYAL SOCIETY OF CHEMISTRY

rsc.li/chemcomm

Registered charity number: 207890

ChemComm

ROYAL SOCIETY OF CHEMISTRY

FEATURE ARTICLE

View Article Online
View Journal | View Issue

Cite this: *Chem. Commun.*, 2023, **59**, 6475

Three-dimensional graphene/metal–organic framework composites for electrochemical energy storage and conversion

Yumei Ren[ab] and Yuxi Xu *[b]

Received 9th March 2023,
Accepted 19th April 2023

DOI: 10.1039/d3cc01167d

rsc.li/chemcomm

Three-dimensional graphene (3DG)/metal–organic framework (MOF)-based composites have attracted more and more attention in the field of energy due to their unique hierarchical porous structure and properties. The combination of graphene with MOFs can not only effectively overcome the limitations of poor electrical conductivity and low stability of MOFs, but also prevent the aggregation and reaccumulation between graphene sheets. Moreover, 3DG/MOF composites can also be used as multifunctional precursors with adjustable structures and composition of derivatives, thus expanding their applications in the field of electrochemistry. This feature article elaborates the latest synthesis methods of 3DG/MOF composites and their derivatives, along with their applications in batteries, supercapacitors (SCs) and electrocatalysis. In addition, the current challenges and future prospects of 3DG/MOF-based composites are discussed.

1. Introduction

The development and utilization of sustainable energy has gradually become an urgent concern. Electrochemical energy storage and conversion systems such as lithium-ion batteries (LIBs) and supercapacitors (SCs) have become one of the most important research fields in the world. Advanced electrode materials are the key to developing new types of high efficiency electrochemical energy storage and conversion devices. As emerging ordered crystal materials, metal–organic frameworks (MOFs) are composed of metal ions or clusters and organic ligands through covalent bonds, coordination bonds and intermolecular forces.[1–4] The variable metal centers and organic ligands of MOFs give them structural and functional diversity.[5–9] Because of their large surface area, high porosity and unique photoelectric effect, MOFs and their derivatives (*i.e.*, porous carbon and metal compounds) have been widely used in the field of electrochemistry.[10–14] However, their low conductivity and poor stability limit their further practical applications to a great extent.[15,16] So far, many efforts have been made to solve these problems. Among them, a promising strategy of combining MOFs with other functional materials to maximize

[a] *School of Materials Science and Engineering, Zhengzhou University of Aeronautics, Zhengzhou 450046, China*
[b] *School of Engineering, Westlake University, Hangzhou 310024, Zhejiang Province, China. E-mail: xuyuxi@westlake.edu.cn*

Yumei Ren

Yumei Ren received her PhD degree from Zhengzhou University in 2018. Now she is works at Zhengzhou University of Aeronautics. Her current research interests focus on the functionalization of 2D materials and their applications in energy conversion.

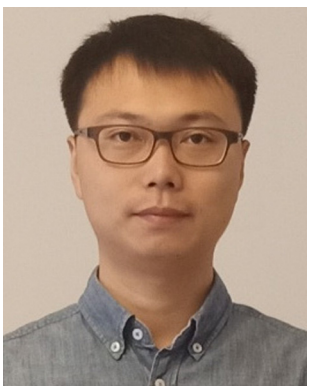

Yuxi Xu

Yuxi Xu received his BS degree from Wuhan University (2007) and PhD degree from Tsinghua University (2011). He then worked as a postdoctoral fellow at the University of California, Los Angeles. He joined the faculty of Fudan University in 2015 and moved to Westlake University in April of 2019. His research interests include chemically modified graphene, 2D polymers, and self-assembled functional materials.

the advantages of the component materials is worthy of careful study, and has attracted widespread attention.[17–19]

Graphene, a typical two-dimensional (2D) layered material with unique physical and chemical properties, has been continuously researched for various applications since 2004.[20–23] Nevertheless, the irreversible agglomeration and restacking of graphene sheets severely suppress its intrinsically outstanding specific surface area, high conductivity, great mechanical strength, *etc.*[24,25] In view of this, three-dimensional graphene (3DG) with a unique porous network structure has currently attracted tremendous attention, as it can not only overcome the strong van der Waals interactions between individual graphene sheets while maintaining the excellent intrinsic properties of graphene, but can also act as the skeleton frame for assembly with other functional materials.[24,26–28] In addition, thanks to its excellent conductivity and high porosity, 3DG is conducive to the transport of electrons and mass during chemical reactions.[25,29,30] However, nanosheets in a pure 3DG network have a high tendency to aggregate or restack during their preparation process and subsequent electrochemical reactions, resulting in a decrease in electrochemical activity.[24,31] Moreover, the extremely low packing density of graphene makes its volume capacitance and energy density low, which limits its further application in the field of electrochemistry.[21] In recent years, many works have proved that the combination of MOFs and 3DG can effectively construct high performance electrode materials for electrochemical energy storage and conversion.[32–36] 3DG/MOF composites and their derivatives can integrate the advantages of their constituent materials, which can not only improve the electrical conductivity and stability of MOFs, but also the structure of MOFs can be optimized through bonding and/or strengthening coordination bonds due to the abundant functional groups of graphene-based materials.[37–39] In addition, 3DG sheets are stable in the existence of MOFs, exposing a larger specific surface area and more active sites. The hierarchical porous structure formed in 3DG/MOF composites is conducive to electrolyte entry and mass transfer resistance reduction, and the close contact between 3DG sheets and MOFs can enhance the adsorption energy and ion transport mechanics, so as to achieve excellent energy storage performance.[28,32]

With the ever-growing efforts into 3DG/MOF-based composites, researchers have paid more attention to their synthesis and applications. Our group has also made some useful exploration in this respect, and has a profound understanding of the current research status and challenges. Although some previous reports have provided excellent overviews of MOF/graphene-based materials, there have been few reviews that focus on the synthesis methods and electrochemical applications of 3DG/MOF composites and their derivatives. In the present feature article, we first summarize the available synthetic methods for 3DG/MOF composites and their derivatives. Then, the application of 3DG/MOF composites and their derivatives in electrochemical energy storage and conversion, including batteries, SCs, and electrocatalysis will be reviewed in detail. Finally, the present challenges and our own perspectives on 3DG/MOF-based composites in the electrochemical research field are discussed.

2. Synthesis of 3DG/MOF composites and their derivatives

Based on the synergy of 3DG and MOFs, the 3DG/MOF-based composites employed as electrode materials show potential advantages in the field of electrochemical energy storage and conversion. To date, many reliable synthesis strategies have been explored to prepare 3DG/MOF composites and their derivatives with diverse architectures (*e.g.*, aerogels, hydrogels, foams, sponges) to meet the requirements of electrochemical applications (Table 1). Generally, the current synthetic routes of 3DG/MOF composites mainly involve two categories: physical mixing and *in situ* growth, while the 3DG/MOF-derived composites including 3DG/MOF-derived carbonaceous materials and metal compounds require further post-treatment processes. In this section, the recent advances in the synthesis of 3DG/MOF-based composites along with their merits and demerits are discussed.

2.1 3DG/MOF composites

2.1.1 Physical mixing. The physical mixing method is a common and simple method for preparing 3DG/MOF composites by directly mechanically mixing presynthesized MOFs and graphene. As an example, Xu and co-workers reported a facial and general method for fabricating a series of 3D GO/MOF aerogels *via* simple vigorous stirring (Fig. 1(a) and (b)).[40] The SEM images shown in Fig. 1(c) and (d) clearly indicate the obtained GO/Fe-MOF and GO/Ni-MOF composite aerogels had highly porous 3D structures and the Fe(Ni)-MOF crystals were uniformly coated on the surface of GO sheets. Recently, Xie *et al.* fabricated a hybrid GO@MIL-101 composite through ultrasonic treatment at room temperature, and the self-assembly of GO and MIL-101 was driven by the electrostatic interactions between them.[41] Similarly, other 3DG/MOF composites, for instance, Co/Zn-MOF@GO, GO/ZIF-67 and ZIF-8/GO have also been successfully constructed in this way.[42–44] Although these routes are simple and feasible, the MOFs and graphene are often dispersed unevenly. In order to solve this problem, the surface of MOFs is usually modified to enhance the interaction between MOFs and graphene. Li and co-workers first functionalized $Co(OH)_2$@PB with a cationic polyelectrolyte poly (diallyldimethylammonium chloride) (PDDA) to make it positively charged, and then a uniform hybrid GO@$Co(OH)_2$@PB was fabricated through the electrostatic interaction between the positively charged $Co(OH)_2$@PB microcubes and negatively charged GO nanosheets.[45] In another work, Ding and co-workers prepared a hybrid structured ZIF-8/GO composite by using cetyl trimethylammonium bromide (CTAB) as the modifier (Fig. 1(e)–(g)).[46] Compared with direct mixing of chemical reagents, hydrothermal treatment is a more efficient way to combine MOFs and GO. Barua *et al.* prepared a graphene-MOF aerogel (GMA) by adding presynthesized CPO-27 into the GO dispersion, followed by a

Table 1 Comparison of the synthesis methods of 3DG/MOF composites and their derivatives

Types	Synthetic strategy	Assisting method	Merits	Demerits	Ref.
3DG/MOF composites	Physical mixing	Stirring/ultrasonication	Easy to perform; facile morphology and size control	Time-consuming; tend toward agglomeration	39–45
	Physical mixing	Hydrothermal	Easy to perform; facile morphology and size control	Tend toward agglomeration	46–49
	In situ growth	Stirring/ultrasonication	Easy to perform; uniform dispersion	Time-consuming; no good shape control and size distribution	53–57
	In situ growth	Hydrogel–organic interfacial diffusion driven	Morphology controllable; can be applied at ambient conditions;	Time-consuming; use organic solvent and post-processing trouble	59
	In situ growth	Water-reflux, freeze drying	Easy to perform; high yields	No good shape control and size distribution	60
	In situ growth	Coprecipitation, ice-template freeze drying	Operation universal and convenient; mass production	No good shape control and size distribution	61
	In situ growth	Hydrothermal/ solvothermal	Simple and adjustable experimental procedures; narrow size distribution and good shape control; high production efficiency	Organic/toxic solvents and high temperature; long reaction times; reaction products are not easy to separate and purify	62–65
	In situ growth	Microwave irradiation induced solvothermal	Short reaction time; highly dispersed and small size; tight junctions	No good shape control and size distribution	66
	In situ growth	CVD, soaking/ hydrothermal	Good purity and high quality	Normally involves multiple steps; high temperature	67–70
	In situ growth	Thermal-assisted spatially confined pulverization	Very narrow size distribution and ultrasmall size	High temperature	71
	In situ growth	Excessive metal-ion induced self-assembly	Facile and controllable; very narrow size distribution and ultrasmall size	Excessive additives, causing other pollution	74–81
3DG/MOF-derived composites	*In situ* growth	Pyrolysis	Narrow size distribution; good shape control and highly scalable	Requirement of high temperature and inert atmosphere	51,72,79,87,95
	In situ growth	Pyrolysis, acid-etching	Control over size and shape and highly scalable	High temperature; post-processing trouble	58,64
	In situ growth	Microwave-assisted thermal conversion	Simple experimental procedure; short reaction time; mass production	Limited control over the size distribution	73,76,80
	In situ growth	Hydrothermal/ solvothermal	Simple and adjustable experimental procedures; narrow size distribution and good shape control; high production efficiency	Organic/toxic solvents and high temperature; long reaction times; reaction products are not easy to separate and purify	49,89

facile hydrothermal reaction at 180 °C for 12 h (Fig. 1(h) and (i)).[47] In previous literature, one more 3DG/MOF composite, such as Fe-Co PBA@GA,[48] In-IPA@rGO,[49] and ZIF-67S@rGO,[50] has been built using this route.

The physical mixing method is easy to manipulate and realize the combination of graphene and MOFs. Since MOFs are prepared separately, their morphology and size can be effectively controlled. However, the fabrication process may be time-consuming, and the relatively weak interaction between graphene and MOFs makes them tend toward agglomeration. Despite some improvements, more efforts are needed to address this problem.

2.1.2 *In situ* growth. The *in situ* method is the most widely used strategy for the preparation of 3DG/MOF composites because the MOFs can uniformly grow *in situ* on graphene deriving from the abundant oxygen-containing functional groups on the surface of graphene (generally GO and rGO), and the interaction between them is strong.[51–53] Based on this characteristic, many studies have been carried out to directly immerse the prepared GO or rGO into the MOF precursors, and then some assistive methods such as stirring,[54,55] ultrasonication,[56–58] self-assembly and hydrothermal/solvothermal[59] are commonly used for *in situ* growth. In a typical case, Sikdar and co-workers directly grew mono/multi-metallic MOF nanocrystals on a porous graphene hydrogel framework using a 'hydrogel–organic interfacial diffusion' driven approach (Fig. 2(a)).[60] The graphene hydrogel-induced bi-phasic (aqueous–organic–gel interfacial) system has been shown to play a key role in the self-assembly of tunable MOF nanostructures. By using this synthesis method, the authors have successfully prepared a variety of MOF based porous graphene aerogel hybrids (MOF-PG), such as $_{AOG}$Cu(BTC)-PG, $_{AOG}$ZIF67-PG, $_{AOG}$ZIF8-PG, and $_{AOG}$TM-PG. The field-emission electron microscopy (FE-SEM) images displayed in Fig. 2(b)–(e) demonstrate that Cu(BTC) MOFs showed a uniform nanowire structure with a few microns length and diameter at ~50–200 nm, and the ZIF67 (the size of ~200–300 nm) and ZIF8 (the size of ~500 nm) MOFs had a typical cubic morphology. Moreover, the TM[R] prepared from the iron nitrate source possessed a rod like structure (length ~400–600 nm and average width ~250 nm). Another report showed that the self-assembly of graphene and MOFs could be performed using a one-pot water-reflux method. Qu *et al.* used this strategy to develop a porous Ni-MOF-74/rGO hybrid by adding the Ni(II)-containing solution to a GO dispersion under continuous stirring and reflux for 2 h, followed by freeze drying to immobilize the loose layered structure (Fig. 2(f)).[61] It was clear that the graphene sheets well coated the uniformly dispersed Ni-MOF-74 nanorods (*ca.* 300 × 1200 nm). Chen *et al.* fabricated a ZIF-67@GO sponge-like precursor *via* a two-step process involving coprecipitation and ice-template freeze drying.[62]

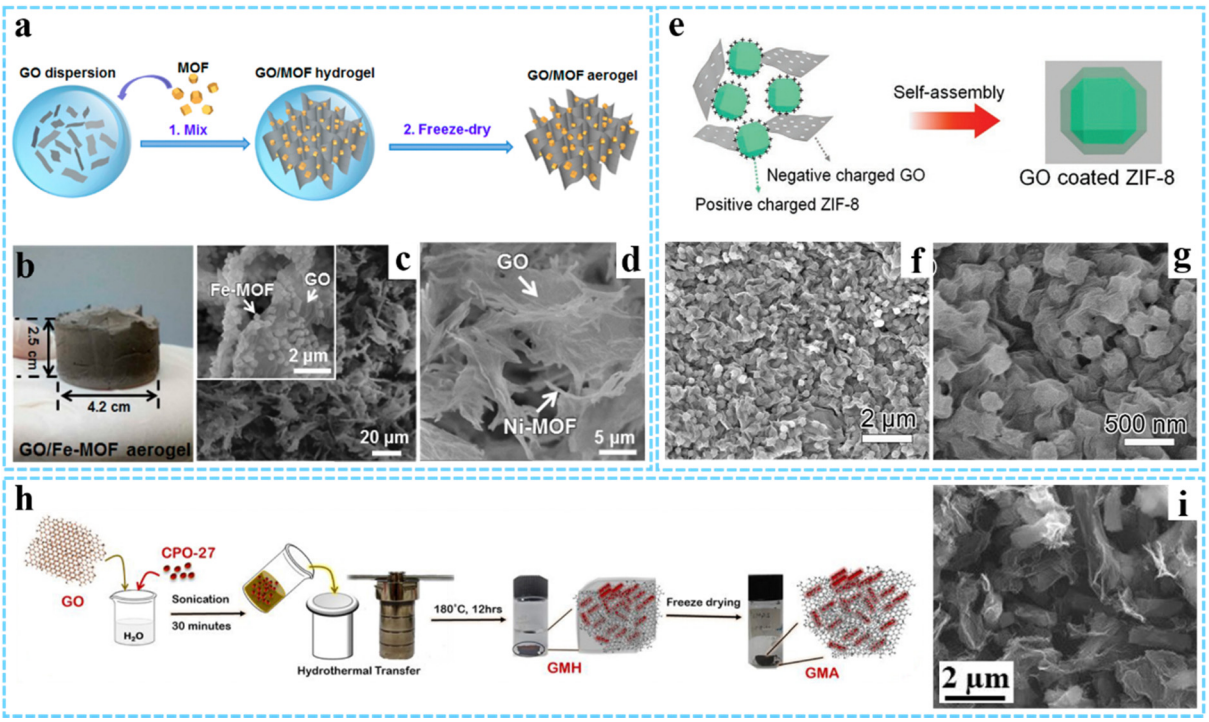

Fig. 1 (a) Schematic of the preparation processes for GO/MOF aerogels. (b) Photographs of the GO/Fe-MOF aerogel. SEM images of (c) GO/Fe-MOF and (d) GO/Ni-MOF composite aerogels. Reprinted with permission from ref. 40. Copyright 2017 American Chemical Society. (e) Schematic illustration of the formation process of the hybrid GO/ZIF-8 composite. (f and g) SEM images of the GO/ZIF-8 composite. Reproduced with permission from ref. 46 Copyright 2019 Wiley-VCH. (h) Synthesis process for GMA. (i) SEM image of GMA. Reprinted with permission from ref. 47. Copyright 2021 American Chemical Society.

Hydrothermal/solvothermal treatment is a common method for preparing functional materials, using water/nonaqueous solvent as the solvent and creating a high-temperature and high-pressure environment after heating. During the hydrothermal/solvothermal reaction, the GO is typically reduced to rGO, and then a 3D cross-linked monolithic graphene network can be formed due to π–π stacking interactions and van der Waals forces between the randomly oriented hydrophobic rGO sheets.[63] For example, Ren and co-workers prepared a 3D nanoflower-like $Co_{0.8}Fe_{0.2}$-MOF-74@rGO hybrid (diameter ~5 μm) *via* a simple hydrothermal reaction (Fig. 2(g) and (h)).[64] Similarly, 3DG/MOF composites with diverse MOF structures have been constructed using such methods, such as GAs-UiO-66-NH_2 (UiO-66-NH_2 crystals with an octahedral cubic intergrown morphology),[65] ADC-rGO (the DMOF-ADC with pillared structure)[66] and 3DGS-CuCo-MOF (the $Co_{3.0}Cu_{1.0}$-MOF with laminated structure)[67] and *etc.* In another study, Wang *et al.* fabricated highly dispersed UIO-66-NH_2 ultrafine nanocrystals *in situ* grown on graphene (UIO-66-NH_2/GR) rapidly with the assistance of a microwave irradiation induced solvothermal route.[68] Besides, using 3DG grown on nickel foam (or directly combined with GO) as the scaffold-supported MOF precursor is also an effective way to improve MOF uniformity, which has been widely used in energy storage and conversion fields.[69–72]

In general, synthesis methods used in the preparation process can not only affect the interaction between MOFs and graphene, but also affect the morphology and properties of the composites. By using conducting polypyrrole (PPy) coated Co-MOFs/GO as precursors, our group successfully fabricated sub-5 nm ultrasmall Co-MOF nanocrystals encapsulated in N-doped carbon/graphene (NC/G) (denoted as GCP350) *via* a facile thermal-assisted spatially confined pulverization strategy (Fig. 2(i)).[73] The GCP350 showed a hierarchical structure with uniformly distributed Co-MOF nanocrystals wrapped by NC/G. The morphology and structure characterization showed that the uniform coating of PPy can significantly improve the decomposition temperature and maintain the component stability of Co-MOFs during calcinations in air, thus leading to the pulverization of bulk Co-MOF particles into ultrasmall nanoparticles (average diameter of ~4.2 nm) without oxidation (Fig. 2(j) and (k)). Without the coating of PPy, Co-MOF particles would transform into metal oxide.

In situ growth can make MOFs produce uniformly on graphene sheets, which can effectively alleviate the agglomeration of MOF nanocrystals and graphene sheets. However, it is not easy to control the growth of MOFs using this method, and the size of MOF nanocrystals is relatively large due to the rapid coordination reaction between metal ions and ligands.

Excess metal-ion induced in situ growth. Considering the special size-dependent properties, small nanomaterials with remarkable properties have attracted wide attention.[74–76] However, the 3DG/MOF composites prepared by the traditional *in situ* growth method usually produce large MOF nanocrystals due to the rapid coordination reaction. To solve this problem,

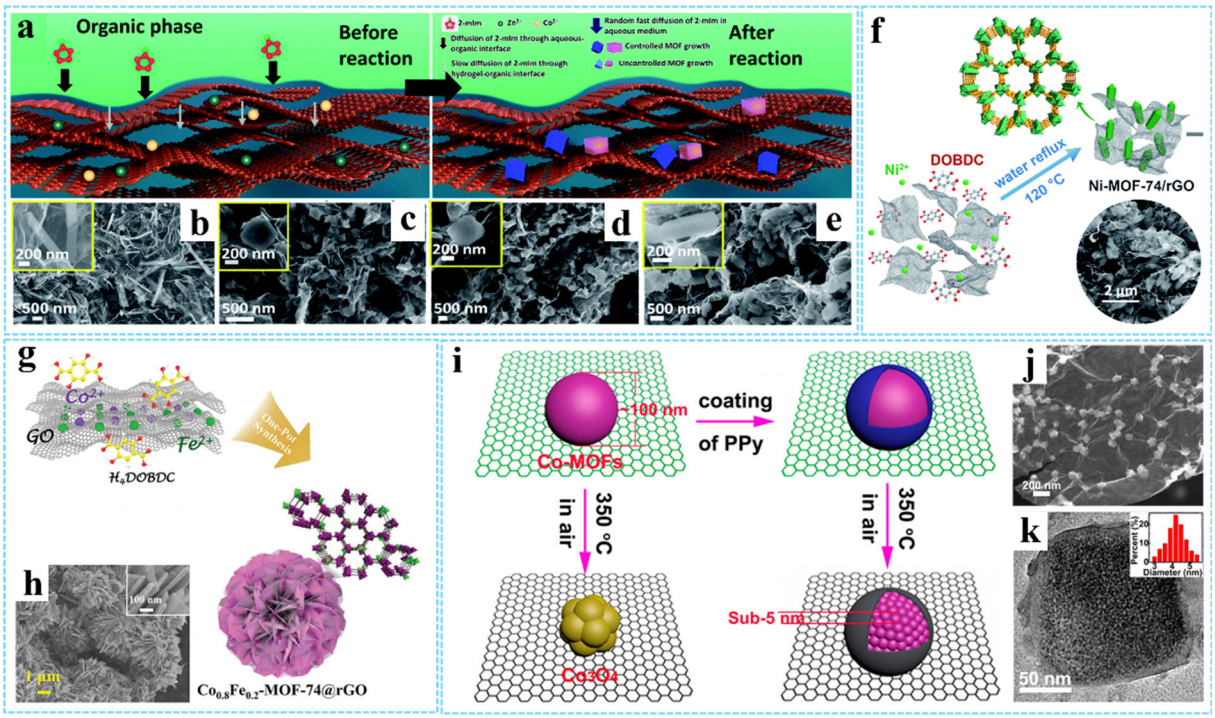

Fig. 2 (a) Schematic for the preparation of MOF-PG hybrids. FESEM images of (b) $_{AOG}$Cu(BTC)-PG, (c) $_{AOG}$ZIF67-PG, (d) $_{AOG}$ZIF8-PG, and (e) $_{AOG}$TM-PG. Reproduced with permission from ref. 60. Copyright 2021 Royal Society of Chemistry. (f) Schematic of the formation process of Ni-MOF-74/rGO. Reproduced with permission from ref. 61. Copyright 2018 Royal Society of Chemistry. (g) Schematic illustration of the synthesis procedure of the $Co_{0.8}Fe_{0.2}$-MOF-74@rGO hybrid. (h) SEM images of $Co_{0.8}Fe_{0.2}$-MOF-74@rGO. Reproduced with permission from ref. 64. Copyright 2020 Wiley-VCH. (i) Schematic diagram of the spatially confined pulverization process of Co-MOFs/GO with and without the coating of PPy. (j) SEM image of GCP350. (k) HRTEM images of GCP350, the inset is a histogram of the size distribution of Co-MOFs nanocrystals. Reprinted with permission from ref. 73. Copyright 2018 American Chemical Society.

our group reported a facile and versatile route for fabricating GO/metal cyanide (GO/MC) composites *via* excess metal-ion induced *in situ* growth (Fig. 3(a)).[77] The experimental results suggested that the excess metal ions were necessary for the successful deposition of MC on GO. The excess metal ions could cover the MC particles and induce the MC particles homogeneity dispersed on GO through coordination interaction and electrostatic attraction and inhibited the overgrowth of MC. In this study, a series of 3DG/MC aerogels such as 3DG/PB, 3DG/Ni–Fe PBA, 3DG/Fe–Co and 3DG/Ni–Ni HCP were successfully obtained by further chemical reduction according to spatially-confined Ostwald ripening. It can be seen that the size of PB nanoparticles before and after adding the sodium ascorbate was around 20 nm and 40–80 nm, respectively (Fig. 3(b) and (c)).

Based on the universality and adjustability of this method, a series of ultrasmall PB or PBA nanoparticles (average size <10 nm) uniformly grown on the GO surface have been reported by us through a modified excessive metal-ion induced self-assembly route (Fig. 3(d)).[78] The resulting PB/GO and PBAs/GO aerogels could be further obtained by freeze-drying. SEM and TEM images shown in Fig. 3(e)–(g) indicate that the average size of the PB nanoparticles was 5.2 nm. Moreover, other ultrasmall PBA nanoparticles, such as Ni–Ni PBA, Ni–Fe PBA, Fe–Co PBA, and FeNi–Co PBA with an average size below 10 nm could also be obtained. Particularly, we have also successfully synthesized other 3DG/MOF composites with a unique structure and excellent properties by using this method.[76,79–83]

In recent years, many 3DG/MOF-based composites have been prepared by direct physical mixing or *in situ* growth, but the choice of MOFs is usually the existing common types, such as the ZIF, MIL and UiO series. Therefore, the variety of MOFs can be expanded by selecting other metal ions and organic ligands. Although the combination of MOFs and graphene can make up for the poor conductivity of MOFs, it will also lose the advantage of MOFs in structural diversity to a certain extent. Thus, the development of new conductive MOFs has broad application prospects.

2.2 3DG/MOF-derived composites

In addition to 3DG/MOF composites, different kinds of nano-sized materials including carbon, metal nanocrystals, and metal compounds (metal oxides, metal sulfides, metal phosphides, *etc.*) derived from MOFs can be introduced into the 3DG to form the hybrids with various morphologies and advanced properties, which are described in the following section.

2.2.1 3DG/MOF-derived carbon materials. MOFs with a porous structure, large surface area and high carbon content are excellent precursors for direct high-temperature carbonization of porous carbon materials (pure porous carbon or metal-doped porous carbon).[84] For pure porous carbon, the metallic elements in MOFs can be evaporated at high temperatures or

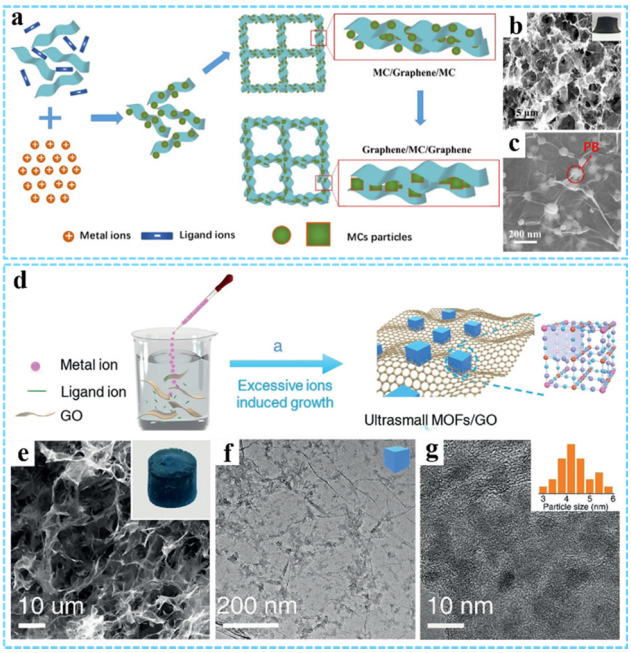

Fig. 3 (a) A schematic illustrating the preparation of the 3DG/MC aerogels. (b) and (c) SEM images of the 3DG/PB aerogel. Reproduced with permission from ref. 77. Copyright 2017 Wiley-VCH. (d) Schematic illustration of the synthesis procedure of ultrasmall MOFs/RGO. (e) SEM and (f and g) TEM images of the PB/GO aerogel. Reproduced with permission from ref. 78. Copyright 2020 Wiley-VCH.

removed by further acid treatment. The simple preparation of MOF-derived carbon materials has the problems of easy carbon material aggregation at high temperature, reduction of active sites and poor electrical conductivity. Combining MOF-derived carbon with graphene can effectively solve these problems, and shows great potential in the field of energy storage and conversion.[46,51,85,86]

Jiao and co-workers firstly synthesized a novel MOF–rGO composite consisting of a nickel-based pillared MOF (DMOF-ADC) and rGO *via* a simple solvothermal method.[66] In the subsequent step, ADC-C/rGO was prepared by further thermal treatment at 600 °C in N_2 and using the concentrated HCl to remove nickel residues, which could be effectively used as the negative electrode material for hybrid supercapacitors (Fig. 4(a)). Morphology and structure characterization indicated that the as-prepared ADC-C/rGO retained a similar morphology to ADC-rGO, and the graphene sheets were uniformly coated on the hollow microrods (Fig. 4(b)). In another study, Wang *et al.* prepared Co, N-codoped porous carbon nanocage anchored 3D graphene framework (Co/N-PCN@rGO) aerogel composites by calcination of ZIF-67@rGO precursor and subsequent partial acid-etching.[59] The ZIF-67 dodecahedron could be transformed into a hollow structure under thermal-induced stress and decomposition. By further HCl (1 M) etching treatment, some Co nanoparticles could be removed, leaving more pores in the system (Fig. 4(c)–(e)). The construction of a porous structure facilitated the penetration of electrolyte, and the strong coupling between Co/N-PCN and rGO was conducive to electron transfer and mechanical stability.

It is well known that the presence of metals can increase the number of active sites and enhance electrical conductivity.[87] When combined with graphene, it shows good activity and excellent stability, and can maintain catalytic activity under strong acidic or alkaline conditions. Considering this, our group has developed a novel, general and ultrafast microwave-assisted thermal conversion strategy, and for the first time prepared a series of M@NC/RGO (FeNi@NC/RGO, CoNi@NC/RGO, Co@NC/RGO, and FeCoNi@NC/RGO) composites by changing the composition of MOF (Fig. 4(f)).[75] This microwave-assisted method broke down the MOF into separate metals and carbon- and nitrogenous gases at the initial thermal conversion stage, rather than producing aggregated metal and carbon composites as conventional heat treatments were carried out, thus effectively controlling the formation of carbon on the metal surface. Finally, uniformly dispersed core@shell M@NC nanocrystals could be formed on graphene sheets, and the averaged size of FeNi@NC, CoNi@NC, Co@NC, and FeCoNi@NC was about 20 nm, 20 nm, 20 nm and 19 nm, respectively (Fig. 4(g)–(k)).

2.2.2 3DG/MOF-derived metal compounds. Metal compounds, such as oxides, sulfides and phosphates, have been shown to possess potential applications in batteries, SCs and electrocatalysis.[88,89] Using MOFs as precursors, metal compounds can be coated in organic ligand-derived carbon materials, so as to obtain dispersed and excellent electrode materials. Due to the unique properties and synergistic advantages of MOFs and graphene, the synthesis and preparation of MOF/graphene-derived metal compounds have attracted extensive attention in recent years, and have been widely used in the field of electrochemistry.

3DG/MOF-derived metal oxides. Using 3DG/MOF composites as precursors, 3DG/MOF-derived metal oxides can be fabricated *via* two-step thermal treatment. Some 3DG/MOF-derived metal oxides (*e.g.*, N-Co_3O_4@N-C/rGO-S,[90] ZnO/3DGN and Fe_2O_3/3DGN,[69] Co_3O_4/3DGN/NF[91]) were produced using this strategy. As an example, Zhu and co-workers prepared a $HoCo_3O_4$/NS-RGO composite with hollow Co_3O_4 nanoparticles embedded in a N,S co-doped rGO framework (Fig. 5(a) and (b)).[92] Firstly, the presynthesized Co-MOF/GO precursor was annealed at 800 °C for 2 h in Ar to obtain the Co@ Co_3O_4/NS-RGO, and the Co@Co_3O_4 possessed a core–shell-like structure with an average diameter of 10–18 nm. Then the resultant $HoCo_3O_4$/NS-RGO composite could be achieved *via* further annealing the Co@ Co_3O_4/NS-RGO in 250 °C air for 2 h. Besides, the corresponding derived metal oxides can also be prepared through a one-step carbonization process in an inert gas.[54,93]

Compared with two-step calcination, one-step calcination in air can effectively shorten the reaction path.[70,94–96] An interesting advance is that our group synthesized a double-holey-heterostructure with the holey Fe_2O_3 nanosheets (H-Fe_2O_3) tightly grown on the holey reduced graphene oxide (H-RGO) by using PB/GO aerogel as the precursor *via* annealing in air (Fig. 5(c) and (d)).[74] TEM results indicated that the continuous holey H-Fe_2O_3 nanosheets were formed through chemically interconnecting the ultrasmall Fe_2O_3 nanoparticles (average diameter ~5 nm) that were generated during the annealing process (Fig. 5(e)). Meanwhile, H-RGO with many nanopores

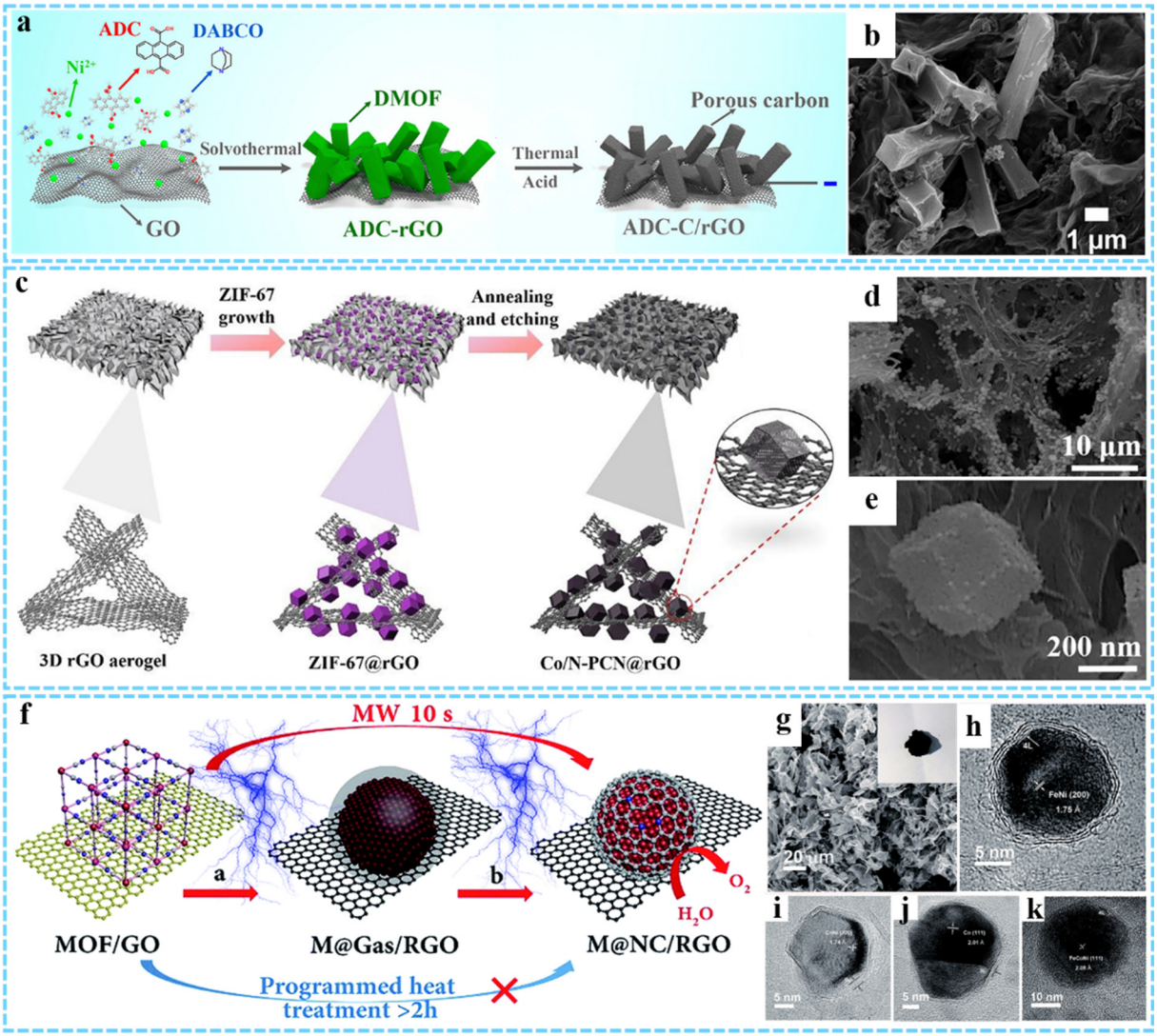

Fig. 4 (a) Illustration of the synthesis process of ADC-C/rGO. (b) SEM image of ADC-C/rGO. Reprinted with permission from ref. 66. Copyright 2019 American Chemical Society. (c) Synthesis procedures for Co/N-PCN@rGO. (d and e) FESEM images of the Co/N-PCN@rGO composites. Reprinted with permission from ref. 59. Copyright 2020 Elsevier. (f) Synthesis process for M@NC/RGO. (g) SEM image of FeNi@NC/RGO. HRTEM images of (h) FeNi@NC/RGO, (i) CoNi@NC/RGO, (j) Co@NC/RGO and (k) FeCoNi@NC/RGO. Reproduced with permission from ref. 75. Copyright 2018 Royal Society of Chemistry.

was produced through the thermal reduction of GO, leading to the thermal degradation of the defective domains on GO. The as-obtained H-Fe_2O_3/H-RGO exhibited a high specific surface area of 280 m^2 g^{-1}, and the abundant nanopores and highly continuous 3D framework allowed for the rapid transfer of ions and electrons when used as an anode for LIBs. By annealing the presynthesized 3DG/PB aerogel at 250 °C for 2 h in air, we successfully fabricated 3DG/Fe_2O_3 aerogel with a porous structure of Fe_2O_3 evenly wrapped within the graphene framework, which was used as the anode for LIBs.[79]

3DG/MOF-derived metal sulfides. Metal sulfides are widely used in the electrochemical field because of their strong conductivity and high specific capacity. The synthesis of metal sulfides using 3DG/MOF composites as the precursor is an effective measure to improve the electrochemical properties, which can not only improve the connectivity between metal sulfides, but also shorten the transport path of ions in the electrolyte path.[33] As a simple and convenient method, 3DG/MOF-derived metal sulfides can be prepared by hydrothermal/solvothermal vulcanization reaction, in which thiourea and thioacetamide (TAA) can be used as sulfur sources.[42,92] He and co-workers successfully prepared Co_9S_8-3DGF composites through a three-step process, including the growth of graphene on nickel foam *via* chemical vapor deposition (CVD), *in situ* growth of MOF on graphene foam, and solvothermal reaction of MOF-3DGF with TAA (Fig. 6(a)).[94] SEM images suggested that Co_9S_8-3DGF with a hollow structure was formed after TAA vulcanization, mainly attributing to the Kirkendall effect (Fig. 6(b)–(d)). Jiang *et al.* designed and prepared a 3D CoS_2QDs@rGO composite *via* a

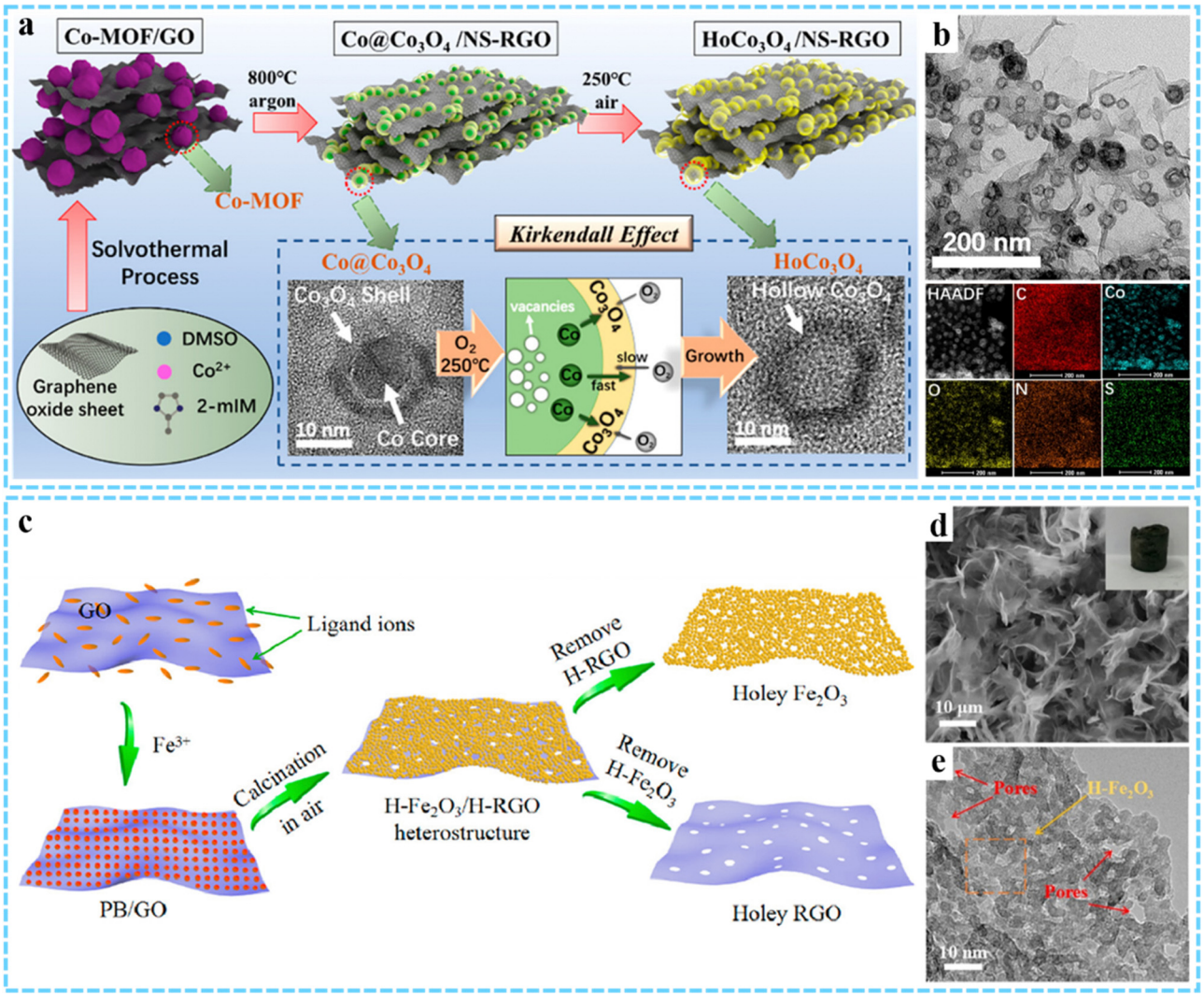

Fig. 5 Schematic of the synthesis process of the $HoCo_3O_4$/NS-RGO framework. (b) TEM and HAADF images of the $HoCo_3O_4$/NS-RGO, along with the corresponding elemental mapping images. Reprinted with permission from ref. 92. Copyright 2020 American Chemical Society. (c) Synthesis procedures for the H-Fe_2O_3/H-RGO heterostructure. (d) SEM and (e) HRTEM images of H-Fe_2O_3/H-RGO. Reprinted with permission from ref. 74. Copyright 2018 American Chemical Society.

two-step hydrothermal method followed by a one-step calcination method, and was used as an efficient catalyst for the hydrogen evolution reaction (HER).[50]

It is an effective method to synthesize metal sulfides by directly calcining the mixture of MOFs and sulfur-containing materials. Inspired by this, using the pre-prepared 3DG/PB aerogel as the precursor, our group designed a new flexible 3DG/FeS@C nanocomposite through one-step thermal conversion after mixing with sulfur powder (Fig. 6(e)).[81] As shown in Fig. 6(f)–(h), the core–shell FeS@C nanocomposite was encapsulated in the 3DG framework, which was formed in the process of sulfur heat treatment derived from 3DG confined phase separation of the metal and organic moieties of PB. The robust 3D porous conductive network together with the core@shell structure and N and S co-doping, which could be directly and effectively used as an anode for sodium-ion batteries (SIBs). Our other work we also successfully prepared FeS_2/PNC@3DG composites using this method.[76] In addition, other 3DG/MOF-derived metal sulfides have been prepared by one-step thermal conversion using sulfur powder or thiourea as sulfur sources.[61,62,97]

3DG/MOF-derived metal phosphides. Due to their high theoretical capacity and activity, metal phosphides have a broad application prospect in the field of electrochemistry.[98] 3DG/MOF-derived metal phosphides have been shown to be one of the most effective strategies to remarkably enhance the electrochemical performance. Different from 3DG/MOF-derived metal sulfides, 3DG/MOF-derived metal phosphides usually choose NaH_2PO_2 as the phosphorus source and can be obtained by one-step calcination in an inert atmosphere.[45,99] For instance, Zhao *et al.* proposed a hierarchical micro/nanostructured hybrid composed of rGO sheets and porous N-doped carbon nanowires constrained CoP nanocrystals (average size ~5.1 nm).[100]

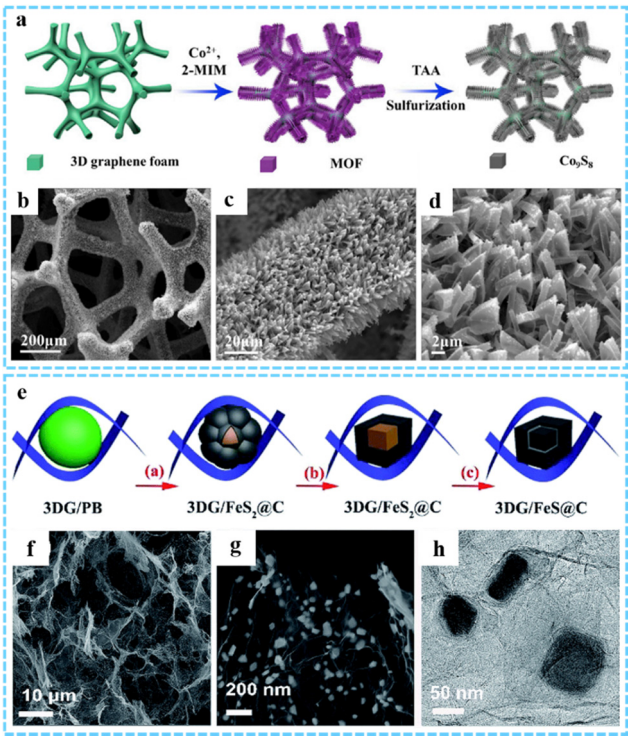

Fig. 6 (a) Schematic illustration of the synthetic route of the Co_9S_8-3DGF composites. (b)–(d) SEM images of Co_9S_8-3DGF. Reprinted with permission from ref. 94. Copyright 2018 Elsevier. (e) Illustration of the synthesis process of the 3DG/FeS@C composites. (f) and (g) SEM and (h) TEM of DG/FeS@C. Reproduced with permission from ref. 81. Copyright 2018 Royal Society of Chemistry.

Zhang *et al.* prepared 3DG/FeP aerogel composites using a spatially confined one-step thermal conversion strategy (Fig. 7(a) and (b)).[101] The FeP nanospheres derived from MOF had hollow structures with an average size of ~50 nm and were evenly coated in graphene sheets (Fig. 7(c) and (d)). Differently, our group have developed a novel ultrafast microwave assisted thermal conversion method and successfully constructed bimetallic phosphide/graphene composites with adjustable heterostructures (Fig. 7(e)).[82] Using NaH_2PO_2 as the phosphorus source, the phosphating reaction of MOF on graphene sheets could be achieved within 20 s under microwave radiation. Through this method, we not only achieved P-doping in graphene to obtain FeNiP/PG composites, but also induced the generation of GC on FeNiP to prepare FeNiP/GC/PG composites, which was very different from traditional heat treatment method (Fig. 7(f) and (h)). The as-obtained FeNiP and FeNiP/GC nanocrystals with an average size of 10 nm and 22 nm were uniformly dispersed on the graphene sheets (Fig. 7(g) and (i)).

3DG/MOF-derived other metal compounds. Due to the variety of metal ions and organic ligands available for MOFs, other MOF-derived metal compounds, such as metal selenides, metal carbides, metal nitrides, *etc.*, can also be prepared by high temperature pyrolysis or other strategies. In order to fabricate the anode for LIBs with excellent performance, we used a 3DG/MOF aerogel as the precursor and subsequently prepared a 3DG/Fe_7Se_8@C composite by calcination with Se powder at 600 °C in Ar/H_2.[80] By using microwave-assisted induced thermal transformation of the PB/GO aerogel, our group achieved the decomposition and transformation of PB to core–shell Fe_3C@C nanoparticles (average size 18 nm) and the reduction of GO to rGO (Fig. 8(a)–(d)).[78] However, under traditional heating conditions, only large and partially aggregated iron/carbon complex (Fe_xC) nanoparticles (average size ~50 nm) could be obtained. In addition, transition metal nitrides (TMNs) have received great attention as electrocatalysts due to their wide range of material types and adjustable surface properties. Using ZIF-67/graphene aerogel (ZIF-67/GA) as a template, Zou and co-workers fabricated a CoN_x/NGA hybrid through thermal treatment at 500 °C in an ammonia atmosphere (Fig. 8(e)–(i)).[52] Due to the abundant active sites of amorphous CoN_x nanoparticles and the 3D porous conductive network structure of NGA, the resultant CoN_x/NGA exhibited excellent electocatalytic activity and stability in the ORR, OER and HER.

So far, a large number of 3DG/MOF-derived composites with complex composition, structure and function have been successfully prepared by high temperature heat treatment. However, the commonly used types of MOFs are still limited. Thus, it is necessary to explore other efficient MOFs as precursors to expand the diversity of MOF derivatives, along with systematically studying the relationship between the properties and structures of MOF-derived materials, which can further guide the design and synthesis of high-performance 3DG/MOF-derived composites. Moreover, most MOF-derived materials need to be calcined at high temperature. Although the 3DG network structure is conducive to the stability of the system, the porous structure can easily be destroyed. Therefore, reasonable reduction of the calcination temperature is also very important for the preparation of high-performance 3DG/MOF-derived composites.

3. Application of 3DG/MOF composites and their derivatives to electrochemical energy storage and conversion

MOFs are known to have high porosity, a large surface area, as well as flexible design and componential diversity, but their poor conductivity and stability limit their wide application in energy storage and conversion. As a typical carbon material, graphene has high electrical conductivity and stability, but graphene sheets tend to aggregate easily. Therefore, combining MOFs with graphene to construct MOF/graphene-based composites can improve their existing problems, so as to synergically promote the electrochemical performance of the system. In this section, we mainly review the applications of 3DG/MOF composites and their derivatives in batteries, SCs and electrocatalysis.

3.1 Batteries

With the rapid development of new energy industries, the development of high-capacity, low-cost and environmentally

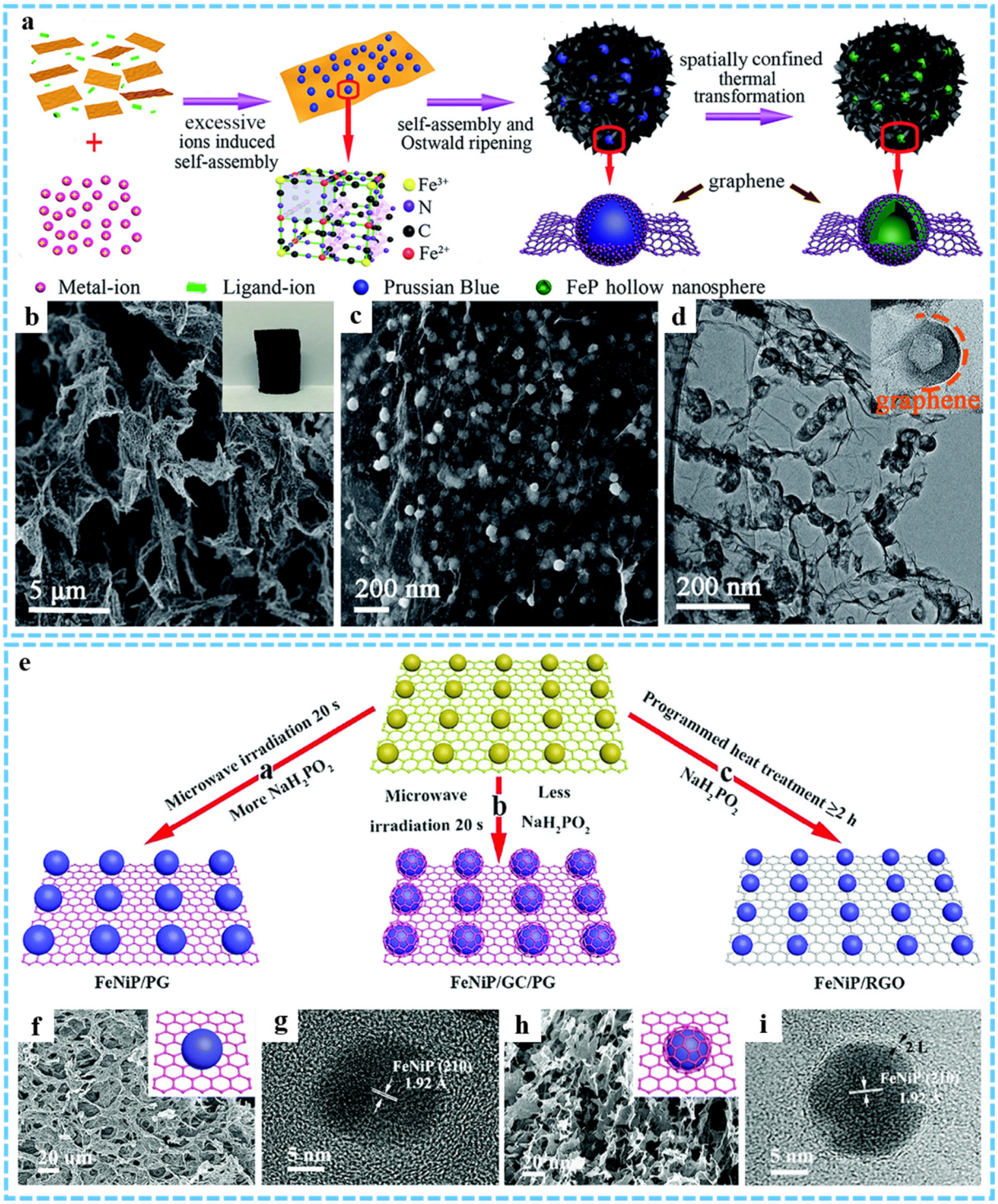

Fig. 7 (a) Synthesis procedures for the 3DG/FeP composite aerogel. (b and c) SEM and (d) TEM images of 3DG/FeP. Reproduced with permission from ref. 101. Copyright 2020 Royal Society of Chemistry. (e) Schematic of the synthetic process of FeNiP/PG, FeNiP/GC/PG and FeNiP/RGO composites. (f) SEM and (g) HRTEM images of FeNiP/PG. (h) SEM and (i) HRTEM images of FeNiP/GC/PG. Reproduced with permission from ref. 82. Copyright 2019 Royal Society of Chemistry.

friendly rechargeable batteries has attracted much attention. As a typical inorganic–organic nanomaterial, MOFs have been widely studied in the construction of battery electrodes due to their special characteristics of large porosity, adjustable structure and abundant active sites.[102] To meet the demand for high performance battery electrode materials, studies have shown that combining MOFs with graphene-based conductive materials can significantly improve the capacity, electronic conductivity and

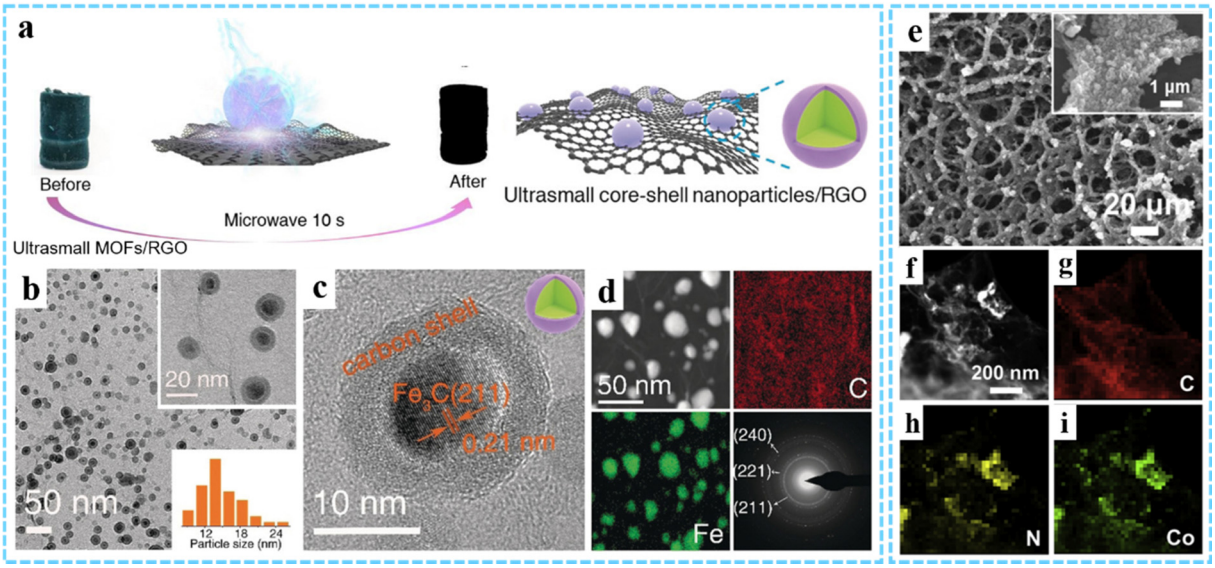

Fig. 8 (a) Schematic illustration of the fabrication process of Fe_3C@C/RGO. (b) TEM and (c) HRTEM images of Fe_3C@C/RGO. (d) STEM image, element mapping and SAED pattern. Reproduced with permission from ref. 78 Copyright 2020 Wiley-VCH. (e) SEM image of CoN_x/NGA. (f) HAADF and (g)–(i) EDXS images of CoN_x/NGA. Reprinted with permission from ref. 52. Copyright 2019 Elsevier.

stability of the system.[103] At present, many researchers have reported the design and synthesis of 3DG/MOF composites and their derivatives with excellent physical and chemical properties for LIBs, SIBs, potassium ion batteries (PIBs) and lithium–sulfur batteries (LSBs) electrode materials.

Lithium-ion batteries. LIBs have been widely used in portable electronic equipment because of their advantages such as large-scale energy storage, long cycle life and good environmental compatibility.[104] In the battery devices, the development of high-performance electrode materials is very important. LIBs work by circulating Li^+ between the positive and negative poles based on the rocking-chair concept.[105,106] Active materials that can reversibly embed and deembed Li^+ are usually selected as cathode and anode materials. In order to improve the energy and power density of LIBs, it is necessary to use anode electrode materials with larger capacity and higher lithium diffusion rate. In recent years, MOF/graphene-based composites with a 3D porous structure show potential advantages. By using the conductive PPy coated Co-MOFs/GO as precursors, our group successfully prepared sub-5 nm ultra-small Co-MOFs nanocrystals encapsulated in GCP350, which was used as an anode material for LIBs (Fig. 9(a)).[73] It exhibited an extremely high reversible capacity of 1301 mA h g^{-1} at 0.1 A g^{-1}, extraordinary rate performance of 494 mA h g^{-1} at 40 A g^{-1}, and excellent cyclic stability with 98.6% capacity maintained after 2000 cycles at 10 A g^{-1} (Fig. 9(b) and (c)). The excellent electrochemical performance of GCP350 benefited from the synergistic effect of ultra-small Co-MOF nanocrystals and 2D ultrathin NC/G layers. Its large specific surface area and abundant active sites was not only conducive to the full contact between electrolyte and active materials, and could shorten the transport distance of Li-ions and electrons, but it also promoted the electron transport.

Based on the excellent structural characteristics of porous and hollow metal oxides derived from MOFs, we designed and synthesized 3DG/Fe_2O_3 composites with porous Fe_2O_3 nanoframeworks,[79] double holey H-Fe_2O_3/H-RGO heterostructure with holey Fe_2O_3 nanosheets,[74] and S-H-Fe_2O_3/RGO composites with ultra-small hollow Fe_2O_3 nanoparticles[78] as high performance anodes for LIBs. In addition, many other 3DG/MOF-derived metal compounds (*e.g.*, 3DG/Fe_7Se_8@C,[80] $HoCo_3O_4$/NS-RGO,[92] Fe_3O_4@C/RGO,[93] NC@CoO_x@GF,[95] PGF@pFe_2O_3 NF,[96] HAGO/Co@CN[43]) have been constructed for LIB electrode materials. For example, Wang *et al.* reported a ZIF-67-derived Co@CN modified horizontally aligned GO array (HAGO/Co@CN) as an independent anode for LIBs.[43] The cross-sectional SEM image showed that the HAGO/Co@CN had a layered porous and highly interpenetrating network structure (Fig. 9(d)). And this unique structure exhibited excellent structural stability and electrochemical performance, which could achieve stable cycling at a high area capacity of 5 mA h cm^{-2} (Fig. 9(e)). In addition, they constructed a full cell with HAGO/Co@CN as the anode and NCM_{622} as the cathode, exhibiting an ultrahigh capacity of 2.3 mA h cm^{-2} at 1 C and a high capacity retention rate (>98%) after 500 cycles (Fig. 9(f) and (g)).

Sodium/potassium-ion batteries. Compared with LIBs, SIBs and PIBs have the same energy storage mechanism and obvious cost advantages, thus showing broad application prospects in large-scale energy storage. However, the radius of Na^+ and K^+ is much larger than that of Li^+, and many electrode materials have poor electrochemical activity and a strong volume expansion effect.[32,33] In view of the current demand for energy storage, developing electrode materials with high specific capacity, good reversibility and long life cycle stability is a major challenge.

Based on the unique advantages of MOFs and graphene, 3DG/MOF-based composites have potential advantages.[45,62,81] Inspired by this, we synthesized a free-standing 3DG/PB aerogel to be used as a cathode material for SIBs, with an excellent rate performance and long-term cycling stability.[77] The remarkable electrochemical properties of the 3DG/PB aerogel derived from

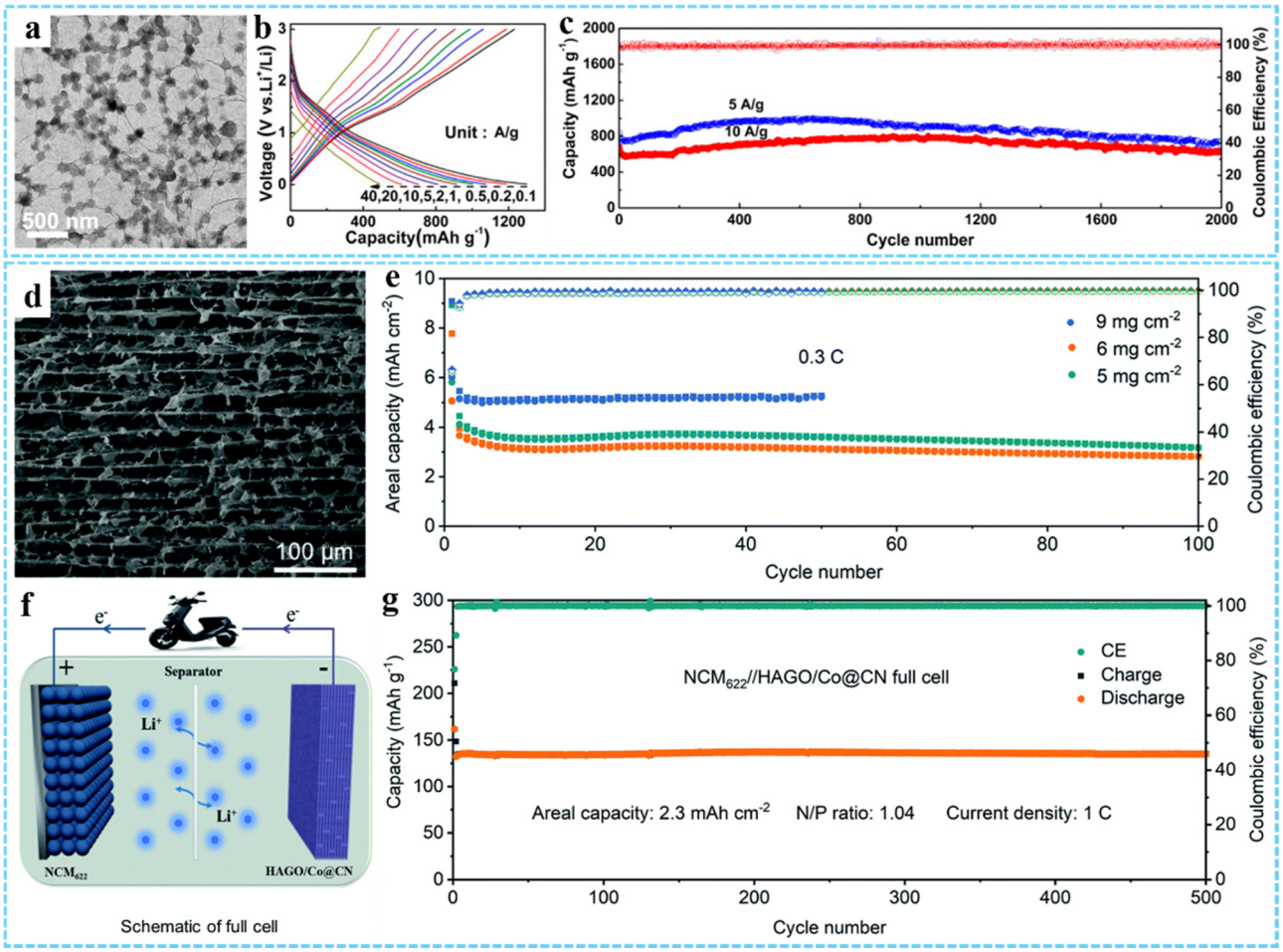

Fig. 9 (a) TEM image of GCP350. (b) Charge–discharge curves of GCP350 at different current densities. (c) Cycling performance of GCP350. Reprinted with permission from ref. 73. Copyright 2018 American Chemical Society. (d) The cross-sectional SEM image of HAGO/Co@CN. (e) Areal capacity of the HAGO/Co@CN electrodes at 0.3C. (f) Schematic diagram of the NCM_{622}//HAGO/Co@CN full cell. (g) Long-term cycle performance of the NCM_{622}//HAGO/Co@CN full cell. Reproduced with permission from ref. 43. Copyright 2022 Royal Society of Chemistry.

their 3D porous conductive frameworks and the special RGO/PB/RGO sandwich structure, resulting in effective electron and ion transport, as well as structural stability. In addition, 3DG/MOF-derived metal compounds have shown great potential in SIBs. Our group explored a multi-scale nanostructured FeS_2/PNC@3DG composite anode using a simple one-step vulcanization strategy.[76] The SEM and TEM results showed that the ultrafine FeS_2 nanocrystals were separated and protected by porous nitrogen-doped carbon nanospheres (PNCS) and uniformly encapsulated in 3DG (Fig. 10(a) and (b)). The unique multi-scale nanostructure of FeS_2/PNC@3DG could increase the active sites, shorten the ion diffusion path, and accelerate the electron/ion transport. Thus, it displayed excellent electrochemical properties, possessing an ultra-high reversible capacity of 597 mA h g^{-1} at 0.2 A g^{-1} (Fig. 10(c)), superior rate capacity of 316 mA h g^{-1} at 5 A g^{-2} (Fig. 10(d)), and excellent long-term cycling performance with a capacity retention of 85.2% after 800 cycles (Fig. 10(e)). Theoretical calculations suggested that the presence of NC not only improved the conductivity of FeS_2, but also provided enhanced Li/Na interface storage. Using ZIF-67-GO-NF as the precursor, Ge *et al.* prepared CoP@C-RGO-NF architectures through a low temperature phosphatizing process, in which the porous core/shell CoP@C polyhedron structures derived from ZIF-67 were uniformly anchored onto the 3D RGO-NF network (Fig. 10(f)).[99] Due to the synergistic effect of porous core/shell structured CoP@C and RGO networks, the specific capacity of CoP@C-RGO-NF as the anode for SIBs could reach 473.1 mA h g^{-1} after 100 cycles at 100 mA g^{-1}, which also showed an excellent reversible capability (Fig. 10(g) and (h)).

PIBs have a higher energy density than SIBs due to the lower reduction potential of K, but the large K^+ radius makes the K^+ reaction kinetics in PIBs slow and the rate performance is not ideal.[35] The construction of porous 3D network electrode materials is considered to be an effective strategy. Our group prepared a Co-MOF-rGO hybrid by using an effective interface engineering strategy, which was employed as the free-standing anode for PIBs (Fig. 11(a)).[83] The strong chemical coupling between Co-MOF and rGO calculated by DFT could improve the adsorption and diffusion of the potassium ion within Co-MOF nanocrystals, rending the Co-MOF-rGO anode with an ultrahigh reversible capacity of 422 mA h g^{-1} at 0.1 A g^{-1}, outstanding

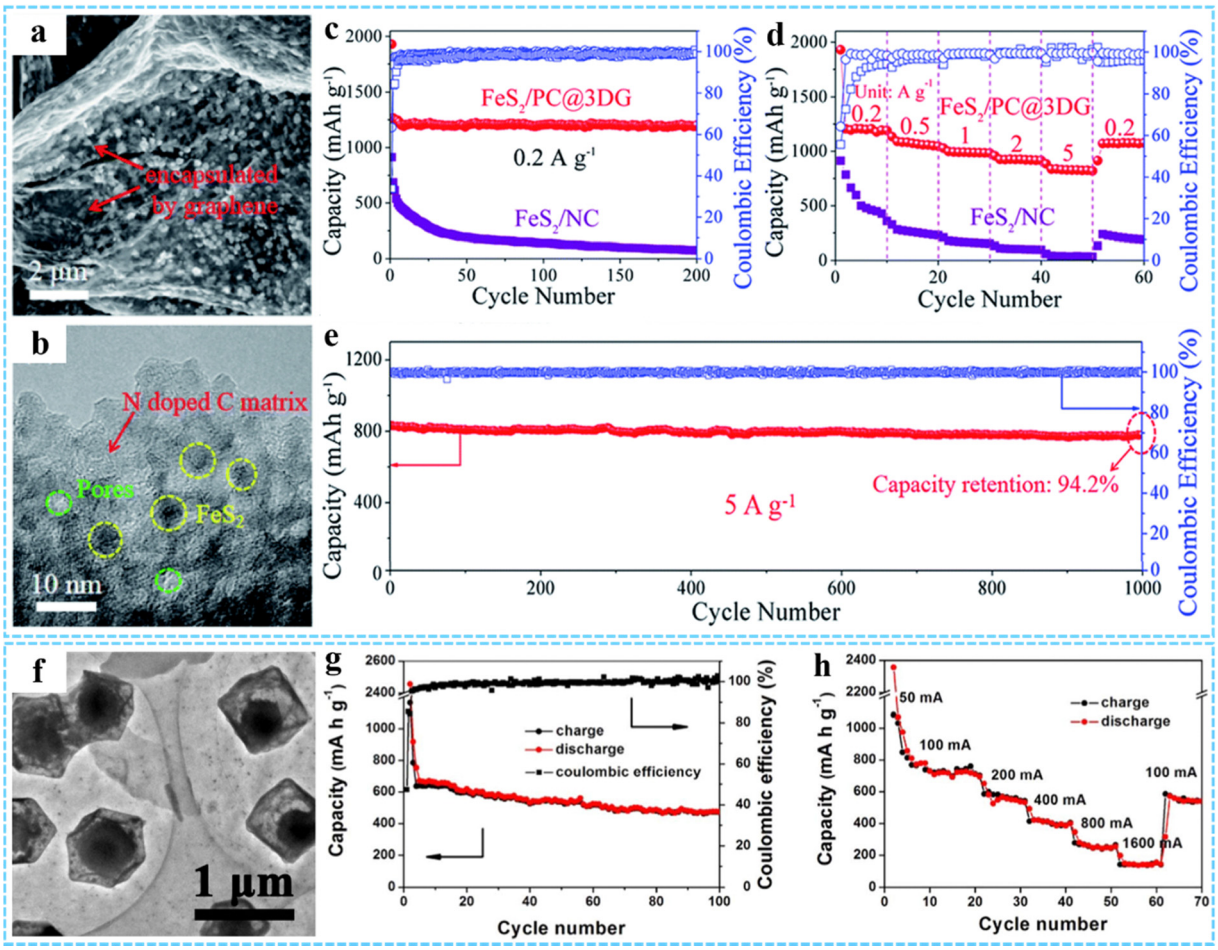

Fig. 10 (a) TEM and (b) HRTEM images of the FeS_2/PNC@3DG aerogel. (c) Cycling performance of the FeS_2/PNC@3DG and FeS_2/NC anode at 0.2 A g^{-1} for 200 cycles. (d) Rate capabilities of the FeS_2/PNC@3DG and FeS_2/NC anodes, respectively. (e) Cycling performance of the FeS_2/PNC@3DG at 5 A g^{-1} for 1000 cycles. Reproduced with permission from ref. 76. Copyright 2019 Royal Society of Chemistry. (f) TEM image of CoP@C-RGO. (g) Cycling performance and coulombic efficiency of the CoP@C-RGO-NF anode at 100 mA g^{-1}. (h) Rate capability of the CoP@C-RGO-NF anode. Reprinted with permission from ref. 99. Copyright 2017 Elsevier.

rate capability of 202 mA h g^{-1} at 5 A g^{-1}, and excellent prolonged cycling performance of 74% capacity retention after 2000 cycles at 2 A g^{-1}, much better than the physical composite Co-MOF/rGO (Fig. 11(b)–(e)). Transition metal phosphides (TMP) have been regarded as promising anode materials for PIBs due to their high theoretical capacity and excellent thermodynamic stability. Using 3DG/MOF as a precursor, Zhang and co-workers constructed a layered porous 3DG/FeP aerogel composite through a spatially confined thermal conversion strategy, in which FeP hollow nanospheres were uniformly encapsulated in the 3DG skeleton (Fig. 11(f)).[101] The electrochemical measurement results showed that the flexible 3DG/FeP film obtained by simple compression of 3DG/FeP aerogel as the anode had a high reversible capacity (323 mA h g^{-1} at 0.1 A g^{-1}) and remarkable electrochemical stability (97.6% capacity retention at 2 A g^{-1} after 2000 cycles) (Fig. 11(g)–(i)).

Lithium–sulfur batteries. Typical LSBs usually have elemental sulfur or sulfur-containing compounds as the cathode and lithium metal as the anode. Due to the abundant resources and high theoretical energy density of the active material sulfur, LSBs with high theoretical specific capacity have attracted much attention.[4,34] However, there are still some problems in LSBs, *e.g.*, the dissolution of polysulfide lithium products in electrolyte, the dendrite growth of lithium metal in the cathode, poor conductivity of sulfur and large volume change during the battery charge/discharge process.[107,108] The design and synthesis of electrode materials with good conductivity, porous flexibility and robustness can effectively improve the above problems. It has been reported that constructing 3DG/MOF-based composites is a good strategy to significantly improve the electrochemical performance of LSBs.[49,59,90] Using ZIF-8/GO composite as the precursor, Ding *et al.* designed and synthesized a 3D porous carbon framework (PCF) containing polyhedral hollow carbon wrapped by RGO through a confined pyrolysis strategy (Fig. 12(a) and (b)).[46] The PCF/S composite electrode obtained by vulcanization as the cathode of LSBs showed a high discharge capacity (1151 mA h g^{-1} at 1C) (Fig. 12(c)) and excellent cycle stability (the capacity decay per cycle is 0.035% during 650 cycles) (Fig. 12(d)). Its excellent electrochemical performance was mainly due to the high conductivity of the constructed 3D porous continuous framework,

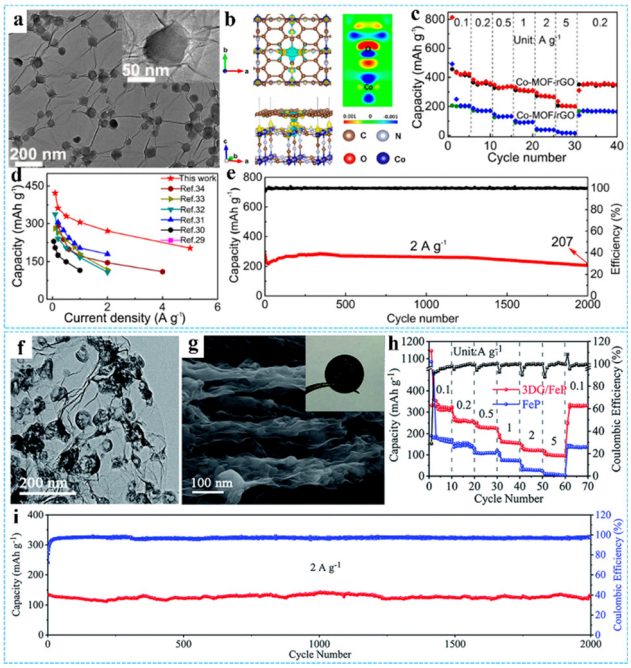

Fig. 11 (a) TEM image of the Co-MOF-rGO hybrid. (b) The charge density difference of the Co-MOF-rGO hybrid. (c) Rate capability of the Co-MOF-rGO and Co-MOF/rGO anodes. (d) Comparison of the Co-MOF-rGO hybrid and other representative anodes of PIB. (e) Long-term cycling performance of Co-MOF-rGO hybrid anodes at 2 A g^{-1} over 2000 cycles. Reprinted with permission from ref. 83. Copyright 2020 American Chemical Society. (f) TEM image of 3DG/FeP. (g) SEM image of the side-view of the pressed 3DG/FeP film, the inset is the photograph of the flexible 3DG/FeP film. (h) Rate performance of 3DG/FeP and FeP. (i) Cycling performance of 3DG/FeP at 2 A g^{-1} for 2000 cycles. Reproduced with permission from ref. 101. Copyright 2020 Royal Society of Chemistry.

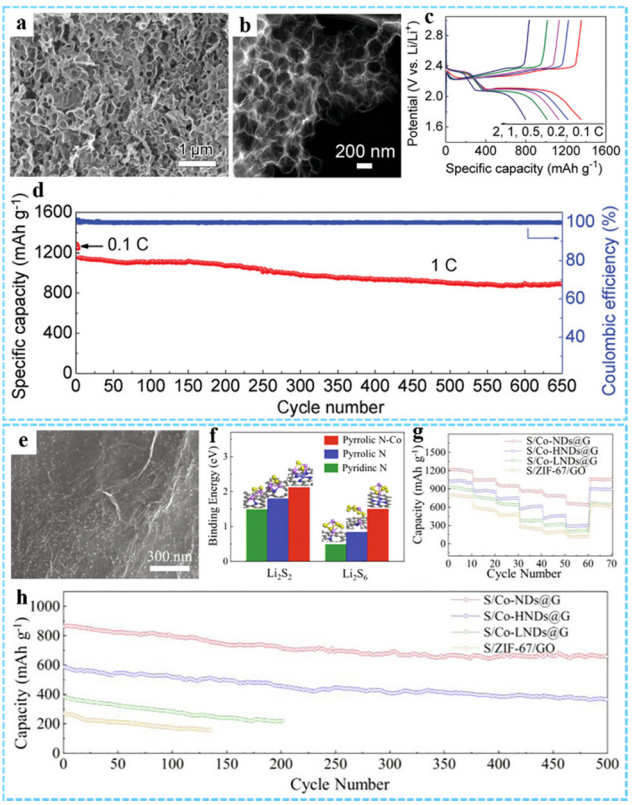

Fig. 12 (a) SEM and (b) STEM images of the PCF. (c) Galvanostatic charge/discharge profiles of the PCF/S electrode at the current densities from 0.1 C to 2 C. (d) The prolonged cycling performance of the PCF/S electrode at 1 C. Reproduced with permission from ref. 46 Copyright 2019 Wiley-VCH. (e) SEM image of Co-NDs@G. (f) Binding energy and optimized structure of Li_2S_2 and Li_2S_6 on Pyridinc N, Pyrrolic N and Pyrrolic N–Co. (g) Multi-rate cycling of cells with the S/Co-NDs@G cathode under raised sulfur loadings. (h) Cycling performance of the Li–S battery at 1C with different cathodes. Reprinted with permission from ref. 87. Copyright 2021 Elsevier.

which could promote the full contact between the active substance and the electrolyte, and its good mechanical stability could adapt to the volumetric expansion/shrinkage of sulfur in the process of charge/discharge. In addition, Wan *et al.* prepared ZIF-67-derived Co nanodots uniformly embedded in 3D graphene aerogel composite (Co-NDs@G) (Fig. 12(e)).[87] Highly dispersed Co nanodots acting as active sites could effectively capture the soluble lithium polysulfides (LiPS), and the strong binding energies between LiPS and the N, Co-doped graphene sheet could accelerate the conversion kinetics of LiPS verified by DFT calculations (Fig. 12(f)), giving it excellent electrochemical activity and stability (Fig. 12(g) and (h)).

3.2 Supercapacitors

As another promising energy storage device, SCs are attracting more and more attention because of their advantages including high power density, fast charging and discharging speed and long cycle life.[109,110] According to the energy storage mechanisms, SCs can be classified into two types: electric double-layer capacitors (EDLCs) that derive from charge separation at the electrode/electrolyte interface and pseudocapacitors that store charge through reversible redox reactions involving the surface region of the electrode material.[111] Generally, EDLCs are composed of carbon-based electrode materials, such as porous carbon, carbon nanotubes and graphene, which exhibit a high power density, long cycle life due to their high specific surface area, controllable porosity, good electron conductivity and so on, but their energy density is low.[112] Conductive polymers and metal compounds are commonly used as pseudocapacitive electrode materials due to their rapid reversible redox reactions, which exhibit higher capacity and energy density.[113] However, their cycle stability is relatively poor and their power density is low. Therefore, thanks to the large specific surface area and potential pseudocapacitor sites of MOFs, as well as electric double-layer capacitance provided by graphene, 3DG/MOF composites have been proven to be highly suitable for using as the SCs electrodes.[41,55] Barua and co-workers prepared a GMA electrode material for supercapacitors without any binder and conductive additive (Fig. 13(a)).[47] The GMA exhibited excellent specific capacitance properties at both low mass loads of 3 mg cm^{-2} (98 F g^{-1} at 0.5 A g^{-1}) and high mass loads of 10 mg cm^{-2} (75 F g^{-1} at 0.5 A g^{-1}) (Fig. 13(b)). In particular,

the GMA electrode showed excellent stability of 100% after 25 000 cycles under both conditions (Fig. 13(c) and (d)). Moreover, Hong *et al.* used a facile one-pot solvothermal method to synthesize a Ni–Co-MOF/GO composite with a 3D structure, and the material used as the capacitor electrode exhibited a high energy storage performance.[56]

Various 3DG/MOF-derived composites have also been employed as promising high-performance SC electrodes, such as Co_3O_4/3DGN/NF,[91] 3DGN/Mn_2O_3,[114] CoO_x/NG-A and C/NG-A,[51] $Co_{1-x}S$/$CoFe_2O_4$@rGO,[64] R-NiS/rGO,[61] Co/Zn–S@rGO,[42] 3D $ZnCo_2O_4$/GA and 3D N-AC/GA,[115] and so on. In a typical case, Xu and co-workers prepared a rGO/Fe_2O_3 aerogel composite through simple freeze-drying and calcination processes of the GO/Fe-MOF composite aerogel precursor (Fig. 13(e)).[40] The specific capacitance of the rGO/Fe_2O_3 electrode reached 869.2 F g^{-1} at 1 A g^{-1}, which was much higher than that of rGO (360.8 F g^{-1}) and Fe_2O_3 (258.5 F g^{-1}) (Fig. 13(f)). When used as a flexible all-solid state supercapacitor, it had a high capacity capacitance and good stability (96.3% capacity retention rate after 5000 cycles) (Fig. 13(g)). The excellent electrochemical performance was mainly due to the 3D framework structures formed by interconnected rGO sheets and the synergistic effect between rGO and Fe-MOF-derived Fe_2O_3 nanostructures. Porous nitrogen-rich carbon and $Ni(OH)_2$ derived from ADC were uniformly anchored on rGO sheets to be used as the negative electrode and positive electrode for SCs individually, as proposed by Jiao and co-workers (Fig. 13(h)).[66] The hybrid device exhibited a high rate capability of 608 C g^{-1} at 1 A g^{-1} and a capacity loss of 5% after 10 000 cycles at 20 A g^{-1} (Fig. 13(i) and (j)).

3.3 Electrocatalysis

Electrocatalysis, as an efficient energy storage and conversion technology, is an important way to achieve sustainable clean energy in the future, among which the HER, oxygen evolution reaction (OER) and oxygen reduction reaction (ORR) are several important reactions in electrochemical energy conversion devices. It is well known that platinum-based materials have excellent electrocatalytic activity, but their high price and low stability limit their commercial application.[37] Therefore, it is

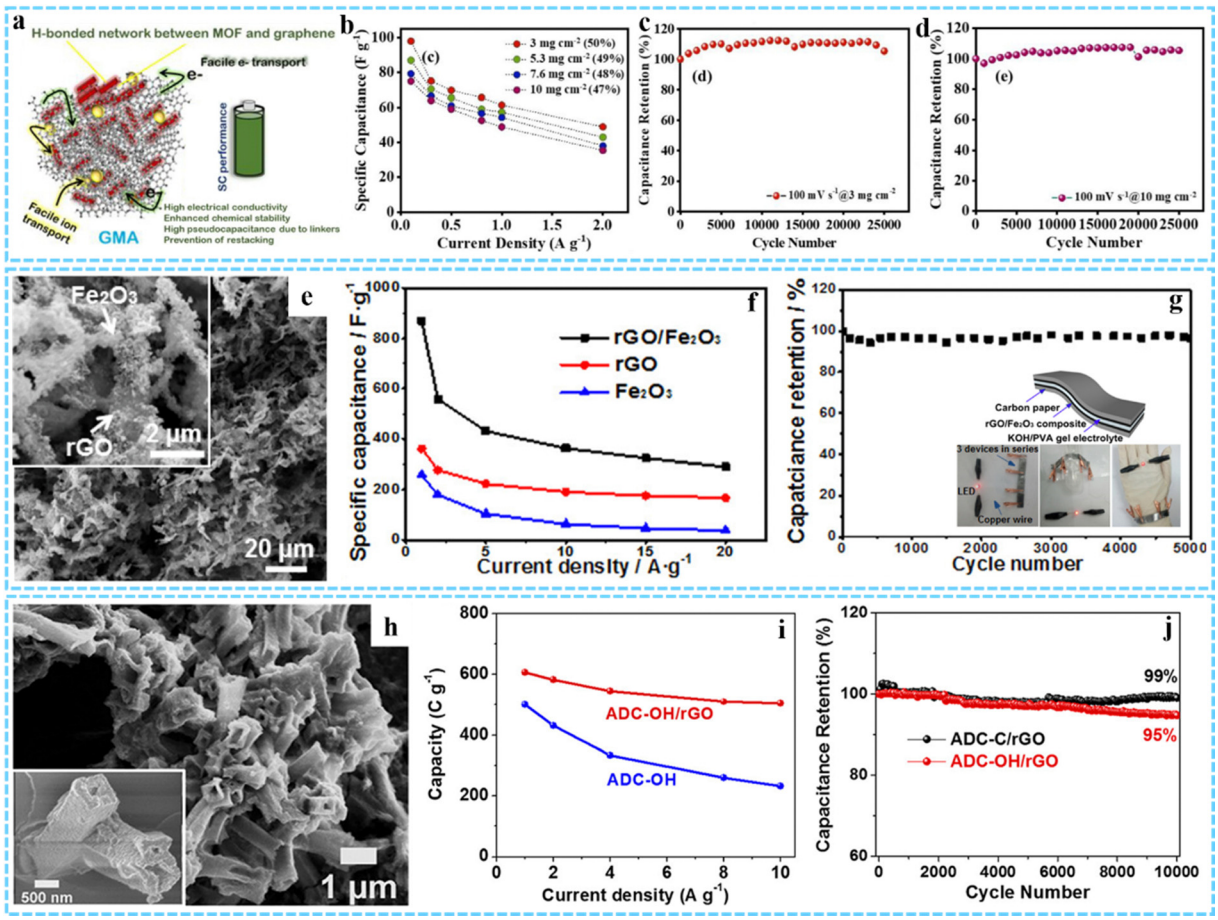

Fig. 13 (a) Schematic illustration of the excellent performance of GMA as a supercapacitor. (b) The specific capacitance retention of GMA at different mass loadings with current density. Cycling performance of GMA at (c) 3 mg cm^{-2} and (d) 10 mg cm^{-2}. Reprinted with permission from ref. 47. Copyright 2021 American Chemical Society. (e) SEM image of the rGO/Fe_2O_3 composite aerogel. (f) Specific capacitance of rGO/Fe_2O_3, rGO, and Fe_2O_3 at different current densities. (g) Long-term cycling performance of the flexible all-solid state supercapacitor based on the rGO/Fe_2O_3 composite. Inset: Schematic diagram of the flexible all-solid state supercapacitor device and the photographs of a red LED lit by a tandem cell. Reprinted with permission from ref. 40. Copyright 2017 American Chemical Society. (h) SEM image of ADC-OH/rGO. (i) Rate performance of ADC-OH and ADC-OH/rGO. (j) Long-term cyclic stability test of ADC-OH/rGO and ADC-C/rGO at 20 A g^{-1}. Reprinted with permission from ref. 66. Copyright 2019 American Chemical Society.

urgent to develop low cost and high performance non-precious metal catalysts. In recent years, 3DG/MOF-based composites have been widely used in the field of electrocatalysts due to their abundant pore structure, large specific surface area, abundant active sites and strong designability.

HER and OER. Electrochemical water splitting to produce hydrogen and oxygen is a promising energy storage technology. HER occurs at the cathode and involves the transfer of two electrons. In the HER, the chemisorption and desorption of H atom on the electrode surface are competitive processes, which play a very key role in the reaction.[116] The OER involves a four-electron transfer and therefore requires a higher thermodynamic potential than the HER to overcome the slow kinetics, which is a key factor limiting the efficiency of water splitting.[117] Thus, the efficiency of electrocatalytic water splitting deeply depends on the choice of electrode materials. In order to improve the activity of the OER, Wang *et al.* designed and synthesized a series of 3DGS/CoCu-MOF composites with bimetallic organic framework grown on a 3D graphene sponge (3DGS) (Fig. 14(a)).[67] 3DGS was characterized by large surface area, high porosity and good electrical conductivity, which could accelerate mass and electron transfer, while the MOF-containing bimetallic active center was used as the catalytic main body. The 3DGS-$Co_{3.0}Cu_{1.0}$-MOF composite showed good electrocatalytic performance with an overpotential of 460 mV, the slope of Tafel curve was 172 mV dec^{-1}, and the charge transfer resistance (R_{ct}) was 16.38 Ω cm^{-2} (Fig. 14(b) and (c)). It also had excellent stability and the current density remained at 95.07% after the test of 20 000 s. There are also many other 3DG/MOF composites that have been used as electrocatalysts for the OER, such as MFN@GA/NF,[71] $Co_{0.3}Ni_{0.7}$-MOF/3DG/NF8,[72] 3D Gr/Ni-MOF,[57] MOF-PG,[60] and so on.

3DG/MOF-derived composites with a unique multilevel network structure, abundant active sites and excellent electrical conductivity can be used as HER and OER electrocatalysts.[36,50,52] Compared with traditional programmed heat treatment, microwave-assisted thermal conversion offers many possibilities for the preparation of novel 3DG/MOF-derived composites.

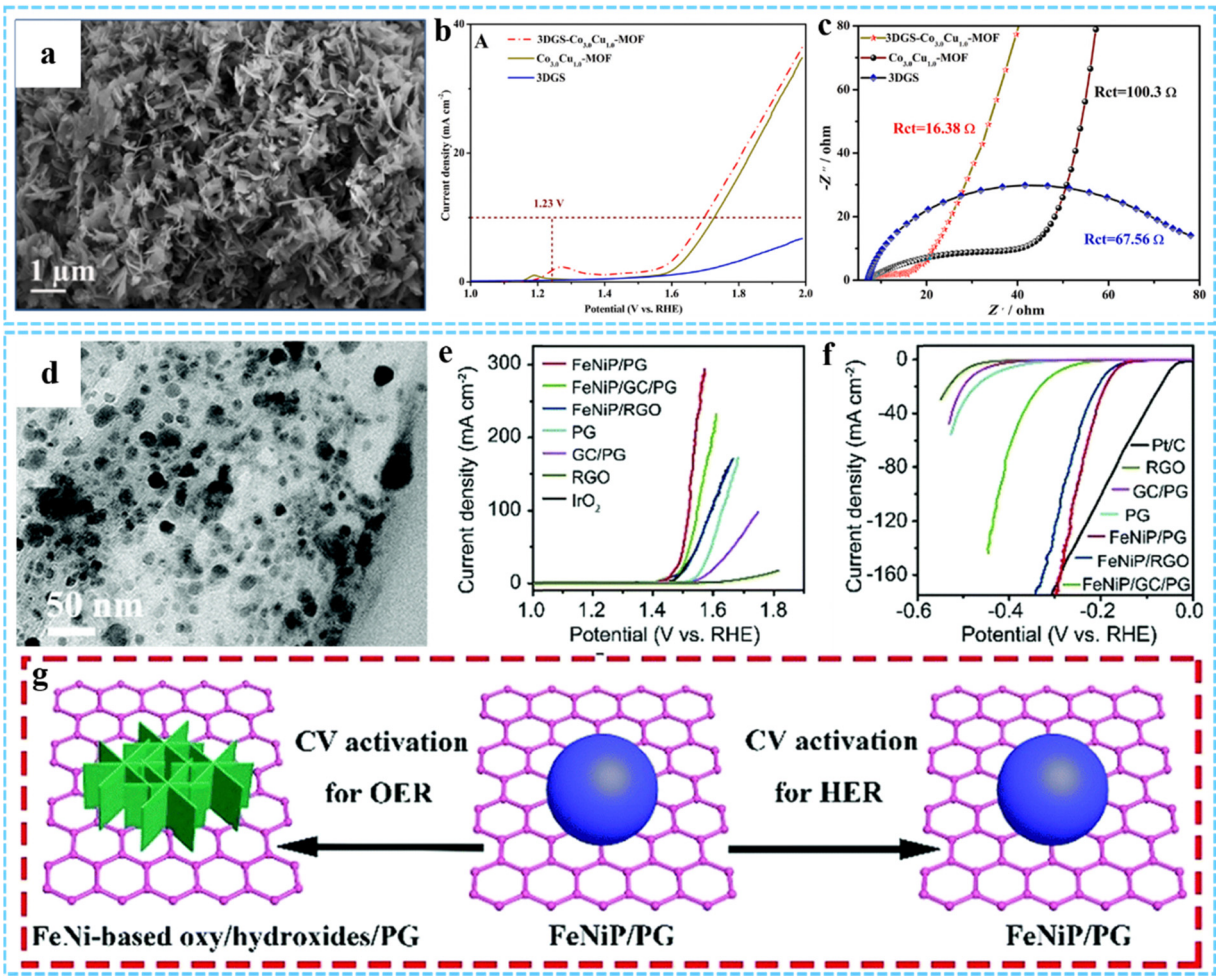

Fig. 14 (a) SEM image of 3DGS-$Co_{3.0}Cu_{1.0}$-MOF. (b) LSV curves and (c) EIS of 3DGS, $Co_{3.0}Cu_{1.0}$-MOF, and 3DGS-$Co_{3.0}Cu_{1.0}$-MOF. Reprinted with permission from ref. 67. Copyright 2021 Elsevier. (d) TEM image of FeNiP/PG. iR-corrected polarization curves of various samples for the (e) OER and (f) HER, respectively. (g) Illustration of morphological changes after the CV activation process of FeNiP/PG for the OER and HER. Reproduced with permission from ref. 82. Copyright 2019 Royal Society of Chemistry.

Using this approach, our group successfully constructed uniformly dispersed monolayer/few-layer N-doped graphene encapsulated metal nanocrystals for efficient electrocatalytic OER.[75] In our other work, we used this method to prepare bimetal phosphide/P-doped graphene (FeNiP/PG) as a bifunctional catalyst for both the OER and HER (Fig. 14(d)).[82] The electrochemical results indicated that FeNiP/PG had low overpotential for the OER (229 mV) and HER (173 mV) at 10 mA cm^{-2} in 1 M KOH solution (Fig. 14(e) and (f)). The morphology of FeNiP/PG did not change significantly during the CV activation process (Fig. 14(g)). Its excellent overall water splitting properties were mainly due to the synergistic effect between FeNiP and PG. The uniformly dispersed FeNiP nanocrystals could provide abundant active sites, and P-doping in graphene could further improve its OER and HER properties.

ORR. The ORR is one of the important reactions of energy conversion and storage in fuel cells and metal–air batteries.[118] It is a multi-electron reaction with very complex reaction mechanism, involving multi-step elementary reaction and different intermediates, and usually has two different pathways of four-electron and two-electron transfer process.[119] The ORR mechanism largely depends on the adsorption behavior of the O_2 molecule on the catalyst surface and determines the rate of the whole electrochemical reaction.[120] As is well known, the quality of electrode materials directly affects the catalytic performance. At present, many non-noble metal electrocatalysts have shown excellent ORR catalytic activity, among which 3DG/MOF composites and their derivatives have the possibility to be used as ORR catalysts due to their unique morphology and ultra-strong adjustability.[54,85,97] Considering that metal oxides and carbon-based materials are promising electrode materials, Xia and co-workers prepared a CoO_x/NG-A composite using Co-based MOF/graphene aerogel as the precursor *via* oxidation treatment in air.[51] HAADF-STEM results showed that the resulting CoO_x hollow nanoparticles (with an external size of ~35 nm and an internal size of ~10 nm) were uniformly dispersed in N-doped graphene aerogels (Fig. 15(a)). Based on the porous N-doped graphene crosslinking network and the rich edge and defect sites of hollow CoO_x, the CoO_x/NG-A showed excellent ORR activity (reduction peak potential of 0.786 V *vs.* RHE, onset potential of 1.019 V, half-wave potential of 54 mV) and stability (no obvious change in polarization curve after 3000 cycles) in 0.1 M KOH solution (Fig. 15(b) and (c)). Yan *et al.* prepared a freestanding 3D CNT/rGO heterostructure film (CGHF) through three steps including solvothermal synthesis of Ni-BTC hollow-microsphere (Ni-BTC HM), vacuum filtration of Ni-BTC HM and GO mixture into film, followed by pyrolysis in Ar (Fig. 15(d)).[121] The Ni-BTC HM-derived CNT microspheres superstructure were connected with rGO, which could effectively prevent the aggregation of rGO sheets. The as-prepared Ni@N-HCGHF with a unique 3D structure possessed large specific surface area, abundant active sites and high conductivity, resulting in significantly improved electrocatalytic activity. As it was used as the OER catalyst, the half-wave potential could reach as high as 0.875 V, and durability tests indicated that the performance loss of it was negligible after a long-term stability test, which was superior to that of Pt/C (Fig. 15(e) and (f)). In addition, it also showed excellent electrocatalytic activity and stability as HER and OER catalysts.

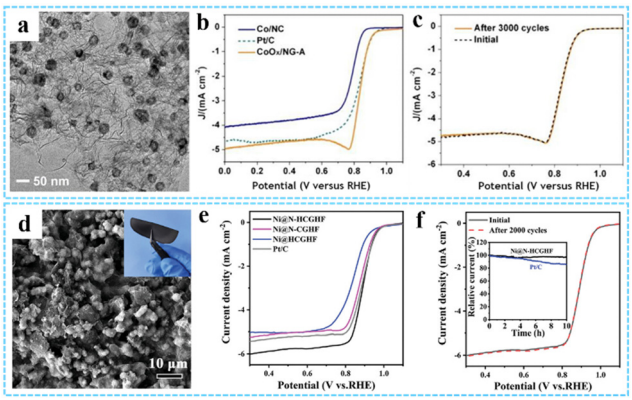

Fig. 15 (a) TEM image of the CoO_x/NG-A composite. (b) ORR polarization curves of CoO_x/NG-A at 10 mV s^{-1} and 1600 rpm. (c) Cycling performance of CoO_x/NG-A. Reprinted with permission from ref. 51. Copyright 2017 American Chemical Society. (d) Top-view SEM image of Ni@N-HCGHF. (e) LSV curves for the ORR of various samples. (f) Cycling performance of Ni@N-HCGHF over 2000 CV cycles. Reproduced with permission from ref. 121 Copyright 2020 Wiley-VCH.

4. Conclusions and prospects

3DG/MOF-based materials with a unique hierarchical porous structure are of great significance to realize high-performance applications in the field of electrochemistry. In this feature article, we first discussed the latest synthesis methods for constructing 3DG/MOF composites (such as physical mixing and *in situ* growth) and 3DG/MOF derivatives. Then, their applications in electrochemical energy storage and conversion fields such as batteries, SCs and electrocatalysis were elaborated in detail.

Although great progress has been made in the preparation and application of 3DG/MOF-based composites recently, there are still some aspects to be further improved and developed. First, currently, the reported types of MOFs are limited, mainly concentrated on ZIF series, MIL series, UiO series and HKUST-1 series. By regulating their composition and structure, more optimized MOFs and their derivatives can be obtained. In addition, other functional MOF-based materials, such as conductive MOFs, have potential advantages in the field of electrochemical applications. Second, for 3D porous materials, the construction of a hierarchical pore structure can simultaneously improve the specific surface area, the number of electrochemical active sites and the efficiency of ion/electron transport. Although 3DG/MOF-based composites exhibit a porous structure, it is difficult to precisely adjust the porous structure, especially for micropores and mesopores. Thus, the preparation of ordered porous 3DG/MOF composites and their derivatives is worth studying. Third, it is well known that strong interaction, coordination effect, synergistic effect and confinement effect at the

interface have an important influence on electrochemical activity and stability. However, the interface interaction between MOFs and graphene is weak. Usually, electrostatic interactions between simple physically mixed MOFs and graphene is enhanced by means of surface modification, and covalent interactions between groups on GO and groups on MOF ligands can be enhanced by *in situ* growth. However, there is competition between oxygen-containing groups on GO and organic ligands on MOFs for the binding of metal cations, which will affect the formation of MOFs. Thus, it is essential to explore 3DG/MOF-based materials with strong interfacial interaction to improve the electrochemical performance. We proposed a facial and versatile strategy for uniform *in situ* growth of MOFs induced by excessive metal ions anchored on the GO surface, which can be extended to the synthesis of other 3DG/MOF-based materials as high performing electrode materials. Fourth, the size and structure of nanomaterials have significant influence on their electrochemical activity. Smaller and monodisperse nanomaterials can provide more active sites, thus promoting the improvement of electrochemical performance. As is known, the synthesis process plays an important role in the structure and morphology of MOFs and their derivatives. We have successfully prepared ultrasmall MOFs and their derivative nanoparticles using excess metal ion-induced self-assembly and subsequent microwave-assisted thermal conversion or space-confined pulverization strategies. This provides an exciting approach for large-scale synthesis of ultrasmall functional MOF nanocrystals, which has a broad application prospect in electrochemical energy storage and conversion. Fifth, the relationship between the structure and properties of 3DG/MOF-based composites still needs to be further studied. The mechanism of electrochemical activity can be systematically and deeply explored by combining advanced characterization techniques and theoretical calculations, so as to provide guidance for the rational design of new high-efficiency electrode materials. We believe that 3DG/MOF composites and their derivatives will show broad prospects in electrochemical energy storage and conversion with continuous progress in the design, preparation and characterization of new materials.

Abbreviations

3DG	Three-dimensional graphene
MOF	Metal–organic framework
SCs	Supercapacitors
LIBs	Lithium-ion batteries
MOFs	Metal–organic frameworks
2D	Two-dimensional
PDDA	Polyelectrolyte poly (diallyldimethylammonium chloride)
CTAB	Cetyl trimethylammonium bromide
GMA	Graphene-MOF aerogel
MOF-PG	MOF based porous graphene aerogel hybrids
FE-SEM	Field-emission electron microscopy
PPy	Polypyrrole
NC/G	N-doped carbon/graphene
GO/MC	GO/metal cyanide
DMOF-ADC	Nickel-based pillared MOF
Co/N-PCN@rGO	Co,N-codoped porous carbon nanocages anchored 3D graphene framework
H-Fe_2O_3	Holey Fe_2O_3 nanosheets
H-RGO	Holey reduced graphene oxide
TAA	Thioacetamide
CVD	Chemical vapor deposition
HER	Hydrogen evolution reaction
SIBs	Sodium-ion batteries
Fe_xC	Iron/carbon complex
TMNs	Transition metal nitrides
ZIF-67/GA	ZIF-67/graphene aerogel
PIBs	Potassium ion batteries
LSBs	Lithium–sulfur batteries
HAGO/Co@CN	ZIF-67-derived Co@CN modified horizontally aligned GO array
PNCS	Porous nitrogen-doped carbon nanospheres
TMP	Transition metal phosphides
PCF	Porous carbon framework
Co-NDs@G	ZIF-67-derived Co nanodots uniformly embedded in 3D graphene aerogel composite
LiPS	Lithium polysulfides
EDLCs	Electric double-layer capacitors
OER	Oxygen evolution reaction
ORR	Oxygen reduction reaction
3DGS	3D graphene sponge
R_{ct}	Charge transfer resistance
FeNiP/PG	Bimetal phosphide/P-doped graphene
CGHF	CNT/rGO heterostructure film
Ni-BTC HM	Ni-BTC hollow-microsphere

Author contributions

All authors contributed to the discussion of the contents and the editing of the manuscript prior to submission.

Conflicts of interest

There are no conflicts to declare.

Acknowledgements

This work was supported by the Natural Science Foundation of Henan Province (no. 202300410488) and the National Natural Science Foundation of China (22022510).

Notes and references

1 L. Jiao, J. Y. R. Seow, W. S. Skinner, Z. U. Wang and H. L. Jiang, *Mater. Today*, 2019, **27**, 43–68.
2 X. H. Cao, C. L. Tan, M. Sindoro and H. Zhang, *Chem. Soc. Rev.*, 2017, **46**, 2660–2677.

3 A. Radwan, H. H. Jin, D. P. He and S. C. Mu, *Nano-Micro Lett.*, 2021, **13**, 132.
4 X. Hu, T. Huang, G. Zhang, S. Lin, R. Chen, L. Chung and J. He, *Chem. Rev.*, 2023, **475**, 214879.
5 S. X. Liu, Z. Y. Teng, H. Liu, T. Y. Wang, G. X. Wang, Q. Xu, X. Y. Zhang, M. Jiang, C. Y. Wang, W. Huang and H. Pang, *Angew. Chem., Int. Ed.*, 2022, **61**, e202207026.
6 J. Jin, W. L. Cai, J. S. Cai, Y. L. Shao, Y. Z. Song, Z. Xia, Q. Zhang and J. Y. Sun, *J. Mater. Chem. A*, 2020, **8**, 3027–3034.
7 D. Cai, M. J. Lu, L. Li, J. M. Cao, D. Chen, H. R. Tu, J. Z. Li and W. Han, *Small*, 2019, **15**, 1902605.
8 W. H. Niu and Y. Yang, *ACS Appl. Energy Mater.*, 2018, **1**, 2440–2445.
9 R. Sahoo, S. Ghosh, S. Chand, S. Chand Pal, T. Kuila and M. C. Das, *Composites, Part B*, 2022, **245**, 110174.
10 J. Xu, Y. Peng, W. Q. Xing, Z. Y. Ding, S. T. Zhang and H. Pang, *J. Energy Storage*, 2022, **53**, 105104.
11 Y. Peng, Y. Bai, C. L. Liu, S. Cao, Q. Q. Kong and H. Pang, *Coord. Chem. Rev.*, 2022, **466**, 214602.
12 W. C. Leng, L. L. Cui, Y. Liu and Y. Gong, *Adv. Mater. Interfaces*, 2022, **9**, 2101705.
13 S. Lyu, C. X. Guo, J. N. Wang, Z. J. Li, B. Yang, L. C. Lei, L. P. Wang, J. P. Xiao, T. Zhang and Y. Hou, *Nat. Commun.*, 2022, **13**, 6171.
14 W. Zhang, W. J. Chen, Q. Xiao, L. Yu, C. Q. Huang, G. X. Lu, A. W. Morawski and Y. Yu, *Appl. Catal., B*, 2020, **268**, 118449.
15 K. Jayaramulu, M. Horn, A. Schneemann, H. Saini, A. Bakandritsos, V. Ranc, M. Petr, V. Stavila, C. Narayana, B. Scheibe, Š. Kment, M. Otyepka, N. Motta, D. Dubal, R. Zbořil and R. A. Fischer, *Adv. Mater.*, 2020, **33**, 2004560.
16 C. W. Gao, P. X. Wang, Z. Y. Wang, S. K. Kær, Y. F. Zhang and Y. Z. Yue, *Nano Energy*, 2019, **65**, 104032.
17 Z. Q. Ye, Y. Jiang, L. Li, F. Wu and R. J. Chen, *Nano-Micro Lett.*, 2021, **13**, 203.
18 Y. Y. Shan, L. Y. Chen, H. Pang and Q. Xu, *Small Struct.*, 2021, **2**, 2000078.
19 W. Xia, J. Tang, J. J. Li, S. H. Zhang, K. C. W. Wu, J. P. He and Y. Yamauchi, *Angew. Chem., Int. Ed.*, 2019, **58**, 1–7.
20 H. J. Huang, M. M. Yan, C. Z. Yang, H. Y. He, Q. G. Jiang, L. Yang, Z. Y. Lu, Z. Q. Sun, X. T. Xu, Y. Bando and Y. Yamauchi, *Adv. Mater.*, 2019, **31**, 1903415.
21 K. F. Chen, S. Y. Song, F. Liu and D. F. Xue, *Chem. Soc. Rev.*, 2015, **44**, 6230–6257.
22 X. H. Xia, D. L. Chao, Y. Q. Zhang, Z. X. Shen and H. J. Fan, *Nano Today*, 2014, **9**, 785–807.
23 Z. H. Chen, X. H. An, L. M. Dai and Y. X. Xu, *Nano Energy*, 2020, **73**, 104762.
24 B. C. Qiu, M. Y. Xing and J. L. Zhang, *Chem. Soc. Rev.*, 2018, **47**, 2165–2216.
25 W. Xiao, B. Li, J. Yan, L. Wang, X. W. Huang and J. F. Gao, *Composites, Part A*, 2023, **165**, 107335.
26 Y. P. Wu, J. H. Zhu and L. Huang, *Carbon*, 2019, **143**, 610–640.
27 S. Mao, G. H. Lu and J. H. Chen, *Nanoscale*, 2015, **7**, 6924–6943.
28 F. X. Bu, I. Shakir and Y. X. Xu, *Adv. Mater. Interfaces*, 2018, **5**, 1800468.
29 G. Z. Li, B. Huang, Z. F. Pan, X. Y. Su, Z. P. Shao and L. An, *Energy Environ. Sci.*, 2019, **12**, 2030–2053.
30 Y. F. Ma and Y. S. Chen, *Nat. Sci. Rev.*, 2015, **2**, 40–53.
31 H. J. Cui, Y. B. Guo and Z. Zhou, *Small*, 2021, **17**, 2005255.
32 K. X. Wang, K. N. Hui, K. S. Hui, S. J. Peng and Y. X. Xu, *Chem. Sci.*, 2021, **12**, 5737–5766.
33 X. Y. Zhang, S. T. Zhang, Y. J. Tang, X. Huang and H. Pang, *Composites, Part B*, 2022, **230**, 109532.
34 M. Y. Zhang, Y. Y. Shan, Q. Q. Kong and H. Pang, *FlatChem*, 2022, **32**, 100332.
35 K. Jayaramulu, S. Mukherjee, D. M. Morales, D. P. Dubal, A. K. Nanjundan, A. Schneemann, J. Masa, S. Kment, W. Schuhmann, M. Otyepka, R. Zbořil and R. A. Fischer, *Chem. Rev.*, 2022, **122**, 17241–17338.
36 M. M. Wang, M. T. Lin, J. T. Li, L. Huang, Z. C. Zhuang, C. Lin, L. Zhou and L. Q. Mai, *Chem. Commun.*, 2017, **53**, 8372–8375.
37 Z. X. Wang, J. Y. Huang, J. J. Mao, Q. Guo, Z. Chen and Y. K. Lai, *J. Mater. Chem. A*, 2020, **8**, 2934–2961.
38 V. Kumari, P. P. Singh and S. Kaushal, *Polyhedron*, 2022, **214**, 115645.
39 S. Li, Y. Liu, J. Zhou, S. Hong, Y. Dong, J. Wang, X. Gao, P. Qi, Y. Han and B. Wang, *Energy Environ. Sci.*, 2019, **12**, 1046–1054.
40 X. L. Xu, W. H. Shi, P. Li, S. F. Ye, C. Z. Ye, H. J. Ye, T. M. Lu, A. A. Zheng, J. X. Zhu, L. X. Xu, M. Q. Zhong and X. H. Cao, *Chem. Mater.*, 2017, **29**, 6058–6065.
41 J. J. Xie, R. Ma, H. B. Fang, H. R. Shi and D. X. Liu, *Cryst. Growth Des.*, 2022, **22**, 2997–3006.
42 N. Xin, Y. Liu, H. T. Niu, H. Y. Bai and W. D. Shi, *J. Power Sources*, 2020, **451**, 227772.
43 Y. Wang, J. W. Li, X. Y. Li, H. Jin, W. J. Ali, Z. X. Song and S. J. Ding, *J. Mater. Chem. A*, 2022, **10**, 699–706.
44 H. S. Choi, Y. H. Kim, H. K. Kim and K. B. Kim, *J. Power Sources*, 2023, **560**, 232702.
45 Z. Q. Li, L. Y. Zhang, X. L. Ge, C. X. Li, S. H. Dong, C. X. Wang and L. W. Yin, *Nano Energy*, 2017, **32**, 494–502.
46 B. Ding, Z. J. Fan, Q. Y. Lin, J. Wang, Z. Chang, T. Li, J. Henzie, J. Kim, H. Dou, X. G. Zhang and Y. Yamauchi, *Small Methods*, 2019, **13**, 1900277.
47 A. Barua, P. Mehra and A. Paul, *ACS Appl. Energy Mater.*, 2021, **4**, 14249–14259.
48 J. X. Shao, J. H. Feng, H. Zhou and A. H. Yuan, *Appl. Surf. Sci.*, 2019, **471**, 745–752.
49 X. C. Jiao, T. Deng, X. L. Men, Y. Z. Zuo and J. Wang, *Ceram. Int.*, 2022, **48**, 16754–16763.
50 J. B. Jiang, R. Sun, X. Huang, H. S. Cong, J. B. Tang, W. X. Xu, M. J. Li, Y. K. Chen, Y. Y. Wang, S. Han and H. L. Lin, *Chem. Eng. J.*, 2022, **430**, 132634.
51 W. Xia, C. Qu, Z. B. Liang, B. T. Zhao, S. G. Dai, B. Qiu, Y. Jiao, Q. B. Zhang, X. Y. Huang, W. H. Guo, D. Dang, R. Q. Zou, D. G. Xia, Q. Xu and M. L. Liu, *Nano Lett.*, 2017, **15**, 2788–2795.
52 H. Y. Zou, G. Li, L. L. Duan, Z. K. Kou and J. Wang, *Appl. Catal., B*, 2019, **259**, 118100.
53 X. Z. Shi, S. A. Zhang, X. C. Chen, T. Tang and E. Mijowska, *Carbon*, 2020, **157**, 55–63.
54 Z. B. Liang, W. Xia, C. Qu, B. Qiu, H. Tabassum, S. Gao and R. Q. Zou, *ChemElectroChem*, 2017, **4**, 2442–2447.
55 A. A. Ensafi, R. Fazel, B. Rezaei and J. S. Hu, *J. Materiomics*, 2022, **8**, 843–851.
56 J. Hong, S. J. Park and S. Kim, *Electrochim. Acta*, 2019, **311**, 62–71.
57 A. J. Xie, J. W. Du, F. Tao, Y. W. Tao, Z. C. Xiong, S. P. Luo, X. Z. Li and C. Yao, *Electrochim. Acta*, 2019, **305**, 338–348.
58 C. F. Meng, P. F. Hu, H. T. Chen, Y. J. Cai, H. Zhou, Z. H. Jiang, X. Zhu, Z. Y. Liu, C. Y. Wang and A. H. Yuan, *Nanoscale*, 2021, **13**, 7751–7760.
59 R. R. Wang, Z. L. Chen, Y. Q. Sun, C. Chang, C. F. Ding and R. B. Wu, *Chem. Eng. J.*, 2020, **399**, 125686.
60 A. Sikdar, A. Majumdar, A. Gogoi, P. Dutta, M. Borah, S. Maiti, C. Gogoi, K. Anki Reddy, Y. Oh and U. N. Maiti, *J. Mater. Chem. A*, 2021, **9**, 7640–7649.
61 C. Qu, L. Zhang, W. Meng, Z. B. Liang, B. J. Zhu, D. Dang, S. G. Dai, B. T. Zhao, H. Tabassum, S. Gao, H. Zhang, W. H. Guo, R. Zhao, X. Y. Huang, M. L. Liu and R. Q. Zou, *J. Mater. Chem. A*, 2018, **6**, 4003.
62 Z. L. Chen, R. B. Wu, M. Liu, H. Wang, H. B. Xu, Y. H. Guo, Y. Song, F. Fang, X. B. Yu and D. L. Sun, *Adv. Funct. Mater.*, 2017, **17**, 1702046.
63 Y. X. Xu, K. X. Sheng, C. Li and G. Q. Shi, *ACS Nano*, 2010, **4**, 4324–4330.
64 C. T. Ren, X. Jia, W. Zhang, D. Hou, Z. Q. Xia, D. S. Huang, J. Hu, S. P. Chen and S. L. Gao, *Adv. Funct. Mater.*, 2020, **30**, 2004519.
65 M. X. Lu, Y. J. Deng, Y. Luo, J. P. Lv, T. B. Li, J. Xu, S. W. Chen and J. Y. Wang, *Anal. Chem.*, 2019, **91**, 888–895.
66 Y. Jiao, C. Qu, B. T. Zhao, Z. B. Liang, H. B. Chang, S. Kumar, R. Q. Zou, M. L. Liu and K. S. Walton, *ACS Appl. Energy Mater.*, 2019, **2**, 5029–5038.
67 H. Y. Wang, A. J. Xie, X. Li, Q. Wang, W. Q. Zhang, Z. R. Zhu, J. H. Wei, D. G. Chen, Y. X. Peng and S. P. Luo, *J. Alloys Compd.*, 2021, **884**, 161144.
68 X. J. Wang, X. L. Zhao, D. Q. Zhang, G. S. Li and H. X. Li, *Appl. Catal., B*, 2018, **228**, 47–53.
69 X. H. Cao, B. Zheng, X. H. Rui, W. H. Shi, Q. Y. Yan and H. Zhang, *Angew. Chem., Int. Ed.*, 2014, **53**, 1404–1409.
70 D. Ji, H. Zhou, Y. L. Tong, J. P. Wang, M. Z. Zhu, T. H. Chen and A. H. Yuan, *Chem. Eng. J.*, 2017, **313**, 1623–1632.
71 C. Chen, J. Z. Wang, P. Li, Q. F. Tian, Z. W. Xiao, S. J. Li, N. Cai, Y. A. Xue, W. M. Chen and F. Q. Yu, *ChemCatChem*, 2021, **13**, 346–352.

72 B. N. Khiarak, M. Hasanzadeh, M. Mojaddami, H. S. Far and A. Simchi, *Chem. Commun.*, 2020, **56**, 3135–3138.
73 P. T. Xiao, F. X. Bu, R. R. Zhao, M. F. A. Aboud, I. Shakir and Y. X. Xu, *ACS Nano*, 2018, **12**, 3947–3953.
74 Z. H. Chen, J. D. Chen, F. X. Bu, P. O. Agboola, I. Shakir and Y. X. Xu, *ACS Nano*, 2018, **12**, 12879–12887.
75 F. X. Bu, W. S. Chen, J. J. Gu, P. O. Agboola, N. F. Al-Khalli, I. Shakir and Y. X. Xu, *Chem. Sci.*, 2018, **9**, 7009–7016.
76 Z. H. Chen, S. Li, Y. Zhao, M. F. A. Aboud, I. Shakir and Y. X. Xu, *J. Mater. Chem. A*, 2019, **7**, 26342–26350.
77 F. X. Bu, X. X. Feng, T. C. Jiang, I. Shakir and Y. X. Xu, *Chem. – Eur. J.*, 2017, **23**, 8358–8363.
78 M. M. Fan, D. K. Liao, M. F. A. Aboud, I. Shakir and Y. X. Xu, *Angew. Chem., Int. Ed.*, 2020, **132**, 8324–8331.
79 T. C. Jiang, F. X. Bu, X. X. Feng, I. Shakir, G. L. Hao and Y. X. Xu, *ACS Nano*, 2017, **11**, 5140–5147.
80 T. C. Jiang, F. X. Bu, B. L. Liu, G. L. Hao and Y. X. Xu, *New J. Chem.*, 2017, **41**, 5121–5124.
81 F. X. Bu, P. T. Xiao, J. D. Chen, M. F. A. Aboud, I. Shakir and Y. X. Xu, *J. Mater. Chem. A*, 2018, **6**, 6414–6421.
82 F. X. Bu, W. S. Chen, M. F. A. Aboud, I. Shakir, J. J. Gu and Y. X. Xu, *J. Mater. Chem. A*, 2019, **7**, 14526–14535.
83 P. T. Xiao, S. Li, C. B. Yu, Y. Wang and Y. X. Xu, *ACS Nano*, 2020, **14**, 10210–10218.
84 H. X. Zhong, J. Wang, Y. W. Zhang, W. L. Xu, W. Xing, D. Xu, Y. F. Zhang and X. B. Zhang, *Angew. Chem., Int. Ed.*, 2014, **53**, 14235–14239.
85 B. Tang, S. K. Wang, R. Li, X. L. Gou and J. L. Long, *J. Power Sources*, 2019, **425**, 76–86.
86 C. X. Li, C. G. Hu, Y. Zhao, L. Song, J. Zhang, R. D. Huang and L. Qu, *Carbon*, 2014, **78**, 231–242.
87 T. T. Wan, S. M. Liu, C. C. Wu, Z. Y. Tan, S. L. Lin, X. J. Zhang, Z. S. Zhang and G. H. Liu, *J. Energy Chem.*, 2021, **56**, 132–140.
88 X. R. Li, X. C. Yang, H. G. Xue, H. Pang and Q. Xu, *EnergyChem*, 2020, **2**, 100027.
89 Y. Zheng, S. S. Zheng, H. G. Xue and H. Pang, *Adv. Funct. Mater.*, 2018, **28**, 1804950.
90 J. Xu, W. X. Zhang, Y. Chen, H. B. Fan, D. W. Su and G. X. Wang, *J. Mater. Chem. A*, 2018, **6**, 2797–2807.
91 X. Y. Deng, J. J. Li, S. Zhu, F. He, C. N. He, E. Z. Liu, C. S. Shi, Q. F. Li and N. Q. Zhao, *Appl. Surf. Sci.*, 2017, **693**, 16–24.
92 J. K. Zhu, W. M. Tu, H. F. Pan, H. Zhang, B. Liu, Y. P. Cheng, Z. Deng and H. N. Zhang, *ACS Nano*, 2020, **14**, 5780–5787.
93 R. X. Jia, R. Zhang, L. B. Yu, X. L. Kong, S. C. Bao, M. Y. Tu, X. H. Liu and B. H. Xu, *J. Colloid Interface Sci.*, 2023, **630**, 86–98.
94 J. R. He, Y. F. Chen and A. Manthiram, *iScience*, 2018, **4**, 36–43.
95 Y. Kong, Y. Luo, J. Ma, J. B. Tang, Y. S. Huang, M. G. Zhou and S. Han, *ACS Appl. Energy Mater.*, 2022, **5**, 5010–5017.
96 J. Ma, Y. Kong, S. C. Liu, Y. T. Li, J. B. Jiang, Q. Y. Zhou, Y. S. Huang and S. Han, *ACS Appl. Energy Mater.*, 2020, **3**, 11900–11906.
97 C. Y. Xie, Q. J. Wang, C. Xiao, L. T. Yang, M. Q. Lan, S. X. Yang, J. W. Xiao, F. Xiao and S. Wang, *Carbon*, 2021, **178**, 640–648.
98 L. M. Cao, D. Lu, D. C. Zhong and T. B. Lu, *Coord. Chem. Rev.*, 2020, **407**, 213156.
99 X. L. Ge, Z. Q. Li and L. W. Yin, *Nano Energy*, 2017, **32**, 117–124.
100 X. J. Zhao, D. Luo, Y. Wang and Z. H. Liu, *Nano Res.*, 2019, **12**, 2872–2880.
101 Z. F. Zhang, C. X. Wu, Z. H. Chen, H. Y. Li, H. J. Cao, X. J. Luo, Z. B. Fang and Y. Y. Zhu, *J. Mater. Chem. A*, 2020, **8**, 3369–3378.
102 X. Xiao, L. L. Zou, H. Pang and Q. Xu, *Chem. Soc. Rev.*, 2020, **49**, 301–331.
103 X. Y. Zhou, S. M. Chen, J. Yang, T. Bai, Y. P. Ren and H. Y. Tian, *ACS Appl. Mater. Interfaces*, 2017, **9**, 14309–14318.
104 L. L. Du, B. Zhang, X. F. Wang, C. H. Dong, L. Q. Mai and L. Xu, *Chem. Eng. J.*, 2023, **451**, 138787.
105 S. A. Han, H. Qutaish, J. W. Lee, M. S. Park and J. H. Kim, *EcoMat*, 2023, **5**, e12283.
106 R. Zhao, Z. B. Liang, R. Q. Zou and Q. Xu, *Joule*, 2018, **2**, 2235–2259.
107 K. Chen, Z. H. Sun, R. P. Fang, Y. Shi, H. M. Cheng and F. Li, *Adv. Funct. Mater.*, 2018, **28**, 1707592.
108 R. J. Chen, T. Zhao, T. Tian, S. Cao, P. R. Coxon, K. Xi, D. Fairen-Jimenez, R. V. Kumar and A. K. Cheetham, *APL Mater.*, 2014, **2**, 124109.
109 W. Du, Y. L. Bai, J. Q. Xu, H. B. Zhao, L. Zhang, X. F. Li and J. J. Zhang, *J. Power Sources*, 2018, **402**, 281–295.
110 Y. M. Ren, C. B. Yu, Z. H. Chen and Y. X. Xu, *Nano Res.*, 2021, **14**, 2023–2036.
111 L. Niu, T. Z. Wu, M. Chen, L. Yang, J. J. Yang, Z. X. Wang, A. A. Kornyshev, H. L. Jiang, S. Bi and G. Feng, *Adv. Mater.*, 2022, **34**, 2200999.
112 L. L. Zhang and X. S. Zhao, *Chem. Soc. Rev.*, 2009, **38**, 2520–2531.
113 R. R. Salunkhe, Y. V. Kaneti and Y. Yamauchi, *ACS Nano*, 2017, **11**, 5293–5308.
114 D. Ji, H. Zhou, J. Zhang, Y. Y. Dan, H. X. Yang and A. H. Yuan, *J. Mater. Chem. A*, 2016, **4**, 8283–8290.
115 P. Xiao, L. J. Cao, H. R. Wang, G. L. Yan and Q. Chen, *Surf. Interfaces*, 2022, **33**, 102266.
116 F. Li, G. F. Han, H. J. Noh, J. P. Jeon, I. Ahmad, S. S. Chen, C. Yang, Y. F. Bu, Z. P. Fu, Y. L. Lu and J. B. Baek, *Nat. Commun.*, 2019, **10**, 4060.
117 S. L. Lyu, C. X. Guo, J. N. Wang, Z. J. Li, B. Yang, L. C. Lei, L. P. Wang, J. P. Xiao, T. Zhang and Y. Hou, *Nat. Commun.*, 2022, **13**, 6171.
118 J. Fu, R. L. Liang, G. H. Liu, A. P. Yu, Z. Y. Bai, L. Yang and Z. W. Chen, *Adv. Mater.*, 2019, **31**, 1805230.
119 X. F. Lu, B. Y. Xia, S. Q. Zang and X. W. (David) Lou, *Angew. Chem., Int. Ed.*, 2020, **132**, 4662–4678.
120 S. Y. Wang, E. B. Zhu, Y. Huang and H. Heinz, *Sci. Adv.*, 2021, **7**, eabb1435.
121 L. T. Yan, Y. L. Xu, P. Chen, S. Zhang, H. M. Jiang, L. Z. Yang, Y. Wang, L. Zhang, J. X. Shen, X. B. Zhao and L. Z. Wang, *Adv. Mater.*, 2020, **32**, 2003313.

